A *cis*-regulatory atlas in maize at single-cell resolution

Alexandre P. Marand[1]*, Zongliang Chen[2], Andrea Gallavotti[2,3], and Robert J. Schmitz[1]*

Affiliations:
[1]Department of Genetics, University of Georgia, Athens, GA 30602, USA
[2]Waksman Institute, Rutgers University, Piscataway, NJ, 08854, USA
[3]Department of Plant Biology, Rutgers University, New Brunswick, NJ, 08901, USA

Correspondence: Alexandre P. Marand (marand@uga.edu), Robert J. Schmitz (schmitz@uga.edu)

ABSTRACT

***Cis*-regulatory elements (CREs) encode the genomic blueprints for coordinating spatiotemporal gene expression programs underlying highly specialized cell functions. To identify CREs underlying cell-type specification and developmental transitions, we implemented single-cell sequencing of Assay for Transposase Accessible Chromatin in an atlas of *Zea mays* organs. We describe 92 distinct states of chromatin accessibility across more than 165,913 putative CREs, 56,575 cells, and 52 known cell-types in maize using a novel implementation of regularized quasibinomial logistic regression. Cell states were largely determined by combinatorial accessibility of transcription factors (TFs) and their associated binding sites. Co-accessible chromatin recapitulated higher-order chromatin interactions, with distinct sets of TFs coordinating cell type-specific regulatory dynamics. Pseudotime reconstruction and alignment with *Arabidopsis thaliana* trajectories identified conserved TFs, associated motifs, and *cis*-regulatory regions specifying sequential developmental progressions. Cell-type specific accessible chromatin regions were enriched with phenotype-associated genetic variants and signatures of selection, revealing the major cell-types and putative CREs targeted by modern maize breeding. Collectively, our analysis affords a comprehensive framework for understanding cellular heterogeneity, evolution, and *cis*-regulatory grammar of cell-type specification in a major crop species.**

50 **MAIN TEXT**

51 Multicellular eukaryote development relies on precise spatiotemporal gene expression mediated
52 by *cis*-regulatory elements (CREs)[1-7]. Despite the economic and nutritional importance of crops
53 to society, our understanding of cell-type functions in plants has been precluded by technical
54 limitations imposed by the cell wall and an inability to culture homogenous cell lines. To
55 circumvent these limitations and comprehensively assess *cis*-regulatory variation among cell-
56 types in a major crop species, we isolated nuclei using fluorescence-activated nuclei sorting
57 (FANS) and generated single-cell accessibility profiles using Assay for Transposase Accessible
58 Chromatin (scATAC-seq) from six major *Zea mays* L. cultivar B73 organs, including axillary buds,
59 staminate and pistillate inflorescence, whole seedling (composed of stem, leaf, and coleoptile
60 tissues), embryonic root tips, and post-embryonic crown roots (**Fig. 1a**, **Extended Data Fig. 1**,
61 **Supplementary Table 1**). Rigorous evaluation of quality metrics, including doublet analysis via
62 genotype mixing (B73/Mo17), biological replicates, per nucleus read-depth, transcription start site
63 (TSS) enrichment, and fragment length distribution were reflective of high-quality scATAC-seq
64 data (Methods, **Extended Data Fig. 1, 2**). In total, we identified 56,575 high-quality nuclei with an
65 average of 31,660 unique Tn5 integration sites per nucleus (**Supplementary Data 1**). To group
66 nuclei with similar global patterns of accessibility, we developed a regularized quasibinomial
67 logistic regression framework that removes technical variation stemming from differences in nuclei
68 read depth by pooling information across accessible chromatin regions (ACRs) and extracting
69 model residuals as normalized accessibility scores for each nucleus and ACR (Methods).
70 Denoising the residual matrix with singular value decomposition (SVD) and projecting the
71 components into a two-dimensional space using Uniform Manifold Approximation Projection
72 (UMAP) revealed 10 clusters generally composed of nuclei from the same organ, highlighting
73 functional diversification of spatially distinct cells (**Fig. 1b, c; Extended Data Fig. 3a-e**). A second
74 round of clustering for each major grouping uncovered a total of 92 sub-clusters (hereafter

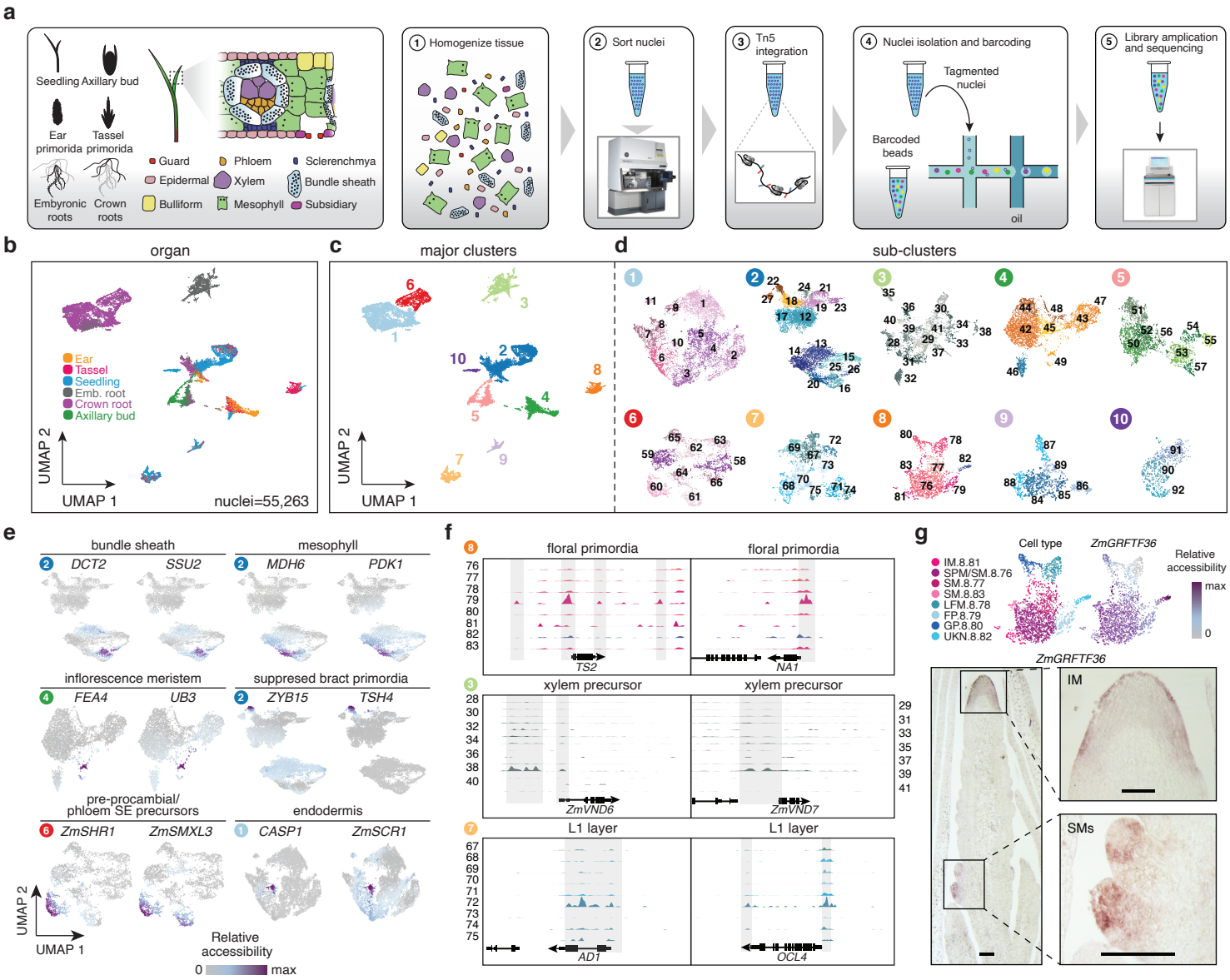

Figure 1: Atlas-scale profiling of single nuclei chromatin accessibility in *Zea mays*

a, Overview of experimental protocol. Homogenized samples release nuclei that are extracted by flow cytometry. Accessible chromatin is tagged by Tn5 and individual nuclei are distinctly barcoded in disparate droplets following microfluidic separation, allowing droplet pooling and library amplification prior to sequencing. **b,** Nuclei similarity clustering as a UMAP embedding derived from the denoised quasibinomial residuals across all ACRs for each nucleus. UMAP embedding of nuclei colored by **b,** organ identity and **c,** major cluster identity. **d,** UMAP embedding of sub-cluster assignments following a second round of clustering within each major cluster. **e,** Cell-type specific enrichment of gene accessibility for a subset of marker genes associated with six different cell-types. **f,** Sub-cluster specific chromatin accessibility profiles surrounding known marker genes for floral primordia, xylem precursors, and L1 epidermal cells. Bold, circled numbers indicate the cognate major cluster shown in panel **c**. Sub-cluster numeric identifications are present on the sides of the coverage plots. **g,** Top, gene accessibility for *ZmGRFTF36*, an inflorescence and spikelet meristem enriched TF with no previously known cell-type specificity. Bottom, RNA in situ hybridization of *ZmGRFTF36* in maize B73 staminate (tassel) primordia. FP, floral primordia; GP, glume primordia; IM, inflorescence meristem; LFM, lower floral meristem; SM, spikelet meristem; SPM, spikelet pair meristem; TF, transcription factor; UKN, unknown.

75 referred to as clusters) with an average of 551 nuclei and 165,913 reproducible ACRs covering
76 ~4% of the maize genome (**Fig. 1d**).

77 To annotate clusters with corresponding cell-types, we integrated gene and promoter (1-
78 kb upstream TSSs) chromatin accessibility information with long-range distal ACRs on the basis
79 of co-accessibility (Methods) into a single accessibility score for each gene and nucleus as a
80 proxy for gene expression (bulk RNA-seq versus aggregate scATAC-seq Spearman's correlation
81 coefficient = 0.54-0.58, **Extended Data Fig. 3f**). We then (*i*) evaluated differential accessibility
82 among clusters for a manually curated list of 221 known marker genes (**Supplementary Table**
83 **2**), (*ii*) classified cell-types of individual nuclei with a multinomial logistic classifier trained on nuclei
84 with discriminative cell-type specific signatures, and visually assessed (*iii*) accessibility scores of
85 *a priori* marker genes over the UMAP embeddings and (*iv*) cluster-aggregated ATAC-seq
86 coverages (Methods, **Fig. 1e**,**f, Extended Data Fig. 4a**, **Supplementary Table 3**). Patterns of
87 gene accessibility were consistent with *a priori* information of cell-type/domain specific
88 expression, such as overlapping accessibility of bundle sheath-specific genes *DICARBOXYLIC*
89 *ACID TRANSPORTER1* (*DCT2*) and *RIBULOSE BISPHOSPHATE CARBOXYLASE SMALL*
90 *SUBUNIT2* (*SSU2*) in bundle sheath cells, and mesophyll-specific genes *MALATE*
91 *DEHYDROGENASE6* (*MDH6*) and *PYRUVATE DEHYDOGENASE KINASE1* (*PDK1*) in
92 mesophyll cells (**Fig. 1e, f, Extended Data Fig. 4a**)[8]. To further corroborate predicted cell-type
93 annotations, we performed RNA in situ hybridization for a subset of differentially accessible genes
94 with no prior evidence of cell-type specificity. In all cases, expression patterns were in line with
95 the predicted localization based on gene accessibility (**Fig. 1g**, **Extended Data Fig. 4b**).
96 Estimates of cell-type proportions within and across organs were also concordant with prior
97 observations, such as the occurrence of vascular bundle sheath and parenchymal mesophyll cells
98 within multiple organs, including those derived from stem and leaf tissues of seedlings and within
99 pistilate and staminate inflorescence (**Extended Data Fig. 4c**, **Supplementary Table 3**)[9].

100 Analysis of chromatin accessibility variation at genic loci revealed 74% (28,625/38,752) of
101 genes with significant differential accessibility (FDR < 0.05, log fold-change > 2), with an average
102 of 2,768 differentially accessible genes per cluster (**Extended Data Fig. 5b, Supplementary**
103 **Data 2**). Marker-agnostic gene set enrichment analysis (GSEA) of Gene Ontology (GO) terms
104 exemplified prior information regarding specific cell-type functions, with enriched terms such as
105 "root hair cell development" in root epidermal initials, "regulation of stomatal closure" in subsidiary
106 cells, and "malate transmembrane transport" for mesophyll cells (**Extended Data Fig. 4d**).
107 Distinct cell-types were generalized by highly specific GO annotations, as most (>51%) GO terms
108 were identified in only a handful of cell-types (five or fewer), implicating accessibility dynamics as
109 underling the signature hallmarks of cell-type identity and function (**Extended Data Fig. 4d**). In
110 summary, this combinatorial approach enabled the identification of 52 cell-types for 83% (76/92)
111 of clusters, capturing nearly all major expected cell-types in the profiled organs and suggesting
112 the existence of novel uncharacterized cell-types present in these data (**Supplementary Table**
113 **3**).
114
115 **Characterization of chromatin accessibility variation**
116 Deconvolution of nuclei into discrete cell-types provides an opportunity to identify CREs encoding
117 cell identity. To this end, we implemented a generalized linear model to catalog ACRs with
118 discrete patterns of chromatin accessibility across cell-types (Methods). In total, 52,520 ACRs
119 (31%) were differentially accessible (FDR < 0.05, fold-change > 2) and restricted to one or a
120 handful of clusters, with an average of 2,826 per-cluster (**Extended Data Fig. 5a**, **6a**, **b**). Similar
121 to the reported functions of transcriptional enhancers in metazoan genomes, we found cluster-
122 specific ACRs were associated with significantly greater enhancer activity based on STARR-seq
123 of maize leaf protoplasts[10] relative to controls (Methods, n=165,913) and non-specific (n=113,393)
124 ACRs (**Fig. 2a**). Deconvolution of chromatin accessibility by cell-type revealed accessible sites
125 primarily located distal to genic regions (>2-kb from any gene) compared to previously published

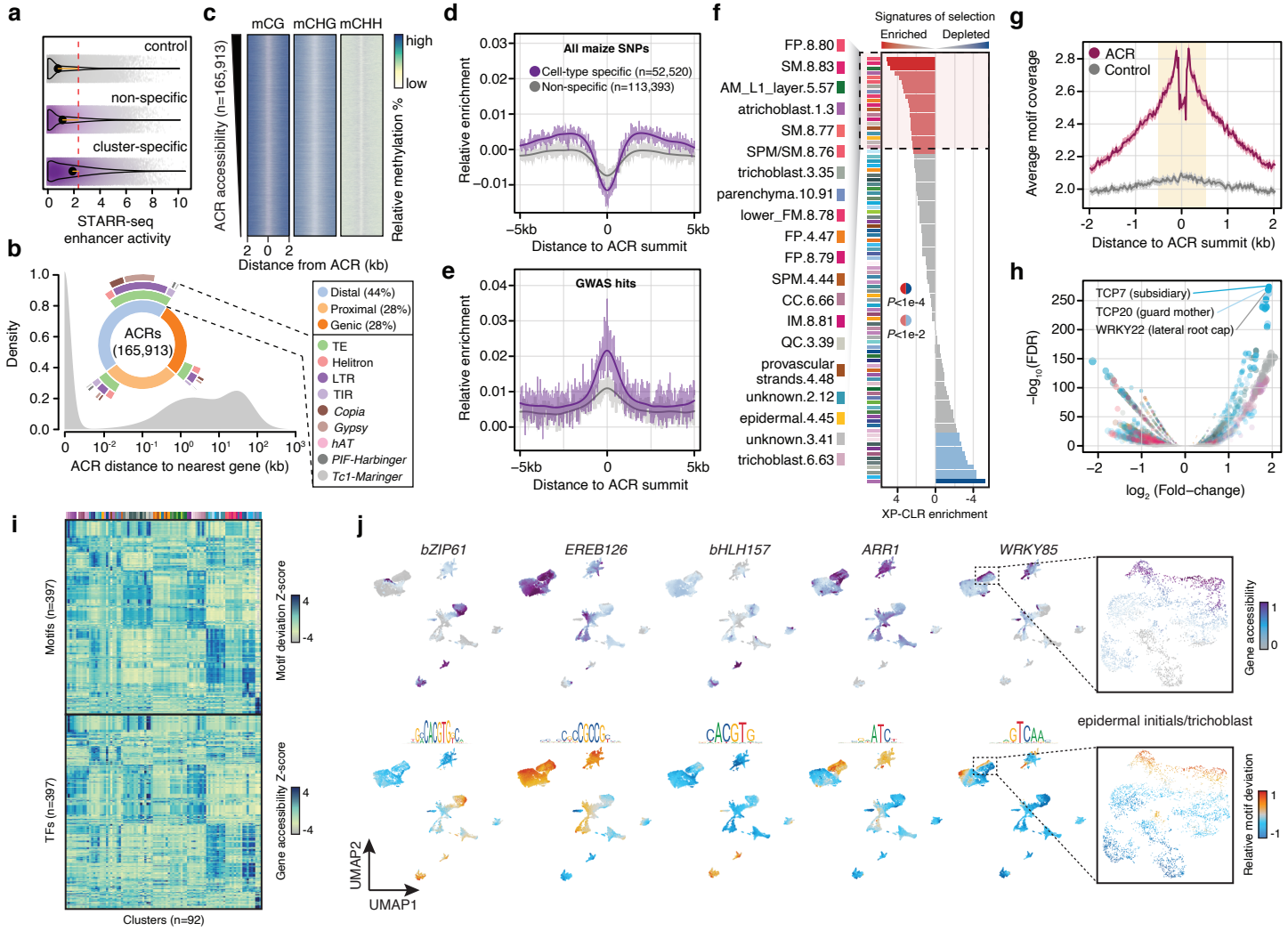

Figure 2: Characterization of accessible chromatin regions

a, Distribution of enhancer activity (maximum log2[RNA/input]) for control regions (n=165,913), non-specific (n=113,393) and cluster-specific ACRs (n=52,520). The dash red line indicates the overall mean. Orange lines reflect differences between the group mean and overall mean. **b,** Distribution of ACR distances to the nearest gene. Inset, distribution of ACR genomic context. **c,** Relative DNA methylation levels 2-kb flanking ACRs. **d,** Relative enrichment of polymorphisms after normalizing by mappability for 5-kb regions flanking cell-type specific and non-specific ACR summits. Smoothed splines are shown as dark lines. **e,** Relative enrichment of significant GWAS polymorphisms relative to all polymorphisms for 5-kb regions flanking cell-type specific and non-specific ACR summits. **f,** Enrichment of signatures of selection (XP-CLR) in the top 2,000 ACRs for all cell-type clusters. The 20 most enriched cell-types are highlighted on the left. AM, axillary meristem; CC, companion cell; FM, floral meristem; FP, floral primordia; IM, inflorescence meristem; QC, quiescent center; SM, spikelet meristem; SPM, spikelet pair meristem. **g,** Average motif coverage for all ACRs (n=165,913) and control regions (n=165,913). Shaded polygon, 95% confidence intervals. **h,** Enrichment of TF motifs in the top 2,000 ACRs ranked by Z-score for each cell-type compared to the top 2,000 most constitutive ACRs via binomial tests. FDR was estimated by the Benjamini-Hochberg method. **i,** Comparative heatmaps for matched TF gene accessibility (bottom) and motif deviation (top) Z-scores across clusters. **j,** Gene accessibility scores for five maize transcription factors (top) and their associated motif deviations (bottom).

126 bulk-level experiments (**Fig. 2b**)[10]. Notably, 30% (22,456/73,791) of distal ACRs overlapped with
127 LTR transposons, including the major maize domestication locus *tb1*-enhancer, and were
128 generally devoid of DNA methylation[11,12]. These findings are consistent with transposable
129 elements playing a prominent role in CRE evolution of the maize genome (**Fig. 2b, c, Extended**
130 **Data Fig. 1a**)[13-15].

131 Sequence variation underlying CREs contribute to disease emergence and phenotypic
132 innovation over evolutionary timescales[16,17]. In contrast to broadly accessible regions, analysis of
133 extant genetic variation in maize revealed lower polymorphism rates within cell-type specific
134 ACRs (**Fig. 2d**). However, of the genetic variants embedded within ACRs, those within cell-type
135 specific ACRs were more frequently associated with phenotypic variation[18] (**Fig. 2e**). To
136 investigate the contribution of domestication and signatures of selection in distinct cell-type
137 contexts, we assessed the relative enrichment of multi-locus allele-frequency differentiation signal
138 (XP-CLR scans) from chronologically sampled elite inbred maize lines within cell-type specific
139 ACRs[19]. Of the 21 cell-types with significant (FDR < 0.01) selection signature enrichment, 57%
140 (12) correspond to staminate and pistillate cell-types, such as spikelet meristems, spikelet pair
141 meristems, inflorescence meristems, floral meristems, and floral primordia (**Fig. 2f**). Thus, modern
142 maize breeding resulted in the selection of alleles containing floral-specific ACRs associated with
143 agronomically favorable inflorescence architecture[20].

144 To characterize the determinants of chromatin accessibility variation among cell-types, we
145 mapped the genome-wide occurrences of 570 transcription factor (TF) motifs. Expectedly, ACRs
146 were highly enriched with putative TF binding sites relative to control (n=165,913) and flanking
147 regions (**Fig. 2g**). Using the top 2,000 differential ACRs for each cell-type, we found 84% of TF
148 motifs (475/568) were enriched (binomial test: FDR < 0.05, Methods) in at least one type, with a
149 median of 43 enriched TF motifs per cell-type (**Fig. 2h**). To characterize TF motif accessibility
150 variation at the scale of individual nuclei, we estimated relative TF motif enrichment controlling for
151 background and sequence bias across ACRs for each nucleus (**Extended Data Fig. 6c-f**).

152 Diverse combinatorial TF motif landscapes were apparent across cell-types and closely mirrored
153 gene accessibility profiles from matched TFs (median PCC across cell-types = 0.45), establishing
154 synchronized chromatin accessibility of *cis* and *trans* cell autonomous factors as major
155 determinants of cell identity (**Fig. 2i, j**, **Extended Data Fig. 6g**). Classification of enriched TFs
156 and their cognate motifs identified several known cell-type specific regulators – including *WRKY*
157 family TFs in root epidermal progenitors and trichoblasts[21], *G2-like1* in parenchymal mesophyll[8],
158 and *AGAMOUS-like* and *SEPALLATA*[22] TFs in floral primordia – as well as previously
159 uncharacterized TFs with new potential roles as cell-type regulators (**Fig. 2i, j**, **Supplementary**
160 **Table 4, 5**). Taken together, these results are indicative of robust inference of CRE and TF activity
161 at the level of single cells and reveal TF dynamics central to *cis*-regulatory specification of diverse
162 cell states.
163
164 **Coordinated dynamic chromatin accessibility recapitulates *in vivo* chromatin interactions**
165 Correlated changes in chromatin accessibility of nearby loci represent putative physical chromatin
166 interactions with regulatory potential[1,23-26]. We identified 3.8 million (M) ACR-ACR linkages
167 (hereafter referred to as co-accessible ACRs) with significantly correlated (empirical FDR < 0.05,
168 Methods) patterns of chromatin accessibility across cell-types, capturing known physical
169 interactions such as between *TB1* and the genetically mapped domestication *tb1*-enhancer that
170 confers inflorescence/axillary meristem-specific expression (**Fig. 3a**, **Extended Data Fig.**
171 **7a**)[10,14,27,28]. To assess the broad interactive potential of co-accessible ACRs *in vivo*, we compared
172 co-accessible ACRs from leaf cell-types with maize whole-leaf chromatin conformation capture
173 data, recovering more than 78% (3,313/4,265), 57% (37,712/65,691) and 44% (17,108/38,567)
174 of chromatin loops from Hi-C, H3K4me3-HiChIP and H3K27me3-HiChIP experiments,
175 respectively (**Extended Data Fig. 7b**). Hi-C/HiChIP is a direct reflection of the proportion of cells
176 exhibiting a particular interaction, as ubiquitously interacting loci dominate rarer cell-type specific
177 contexts that are frequently missed by loop-calling algorithms. To determine the relative

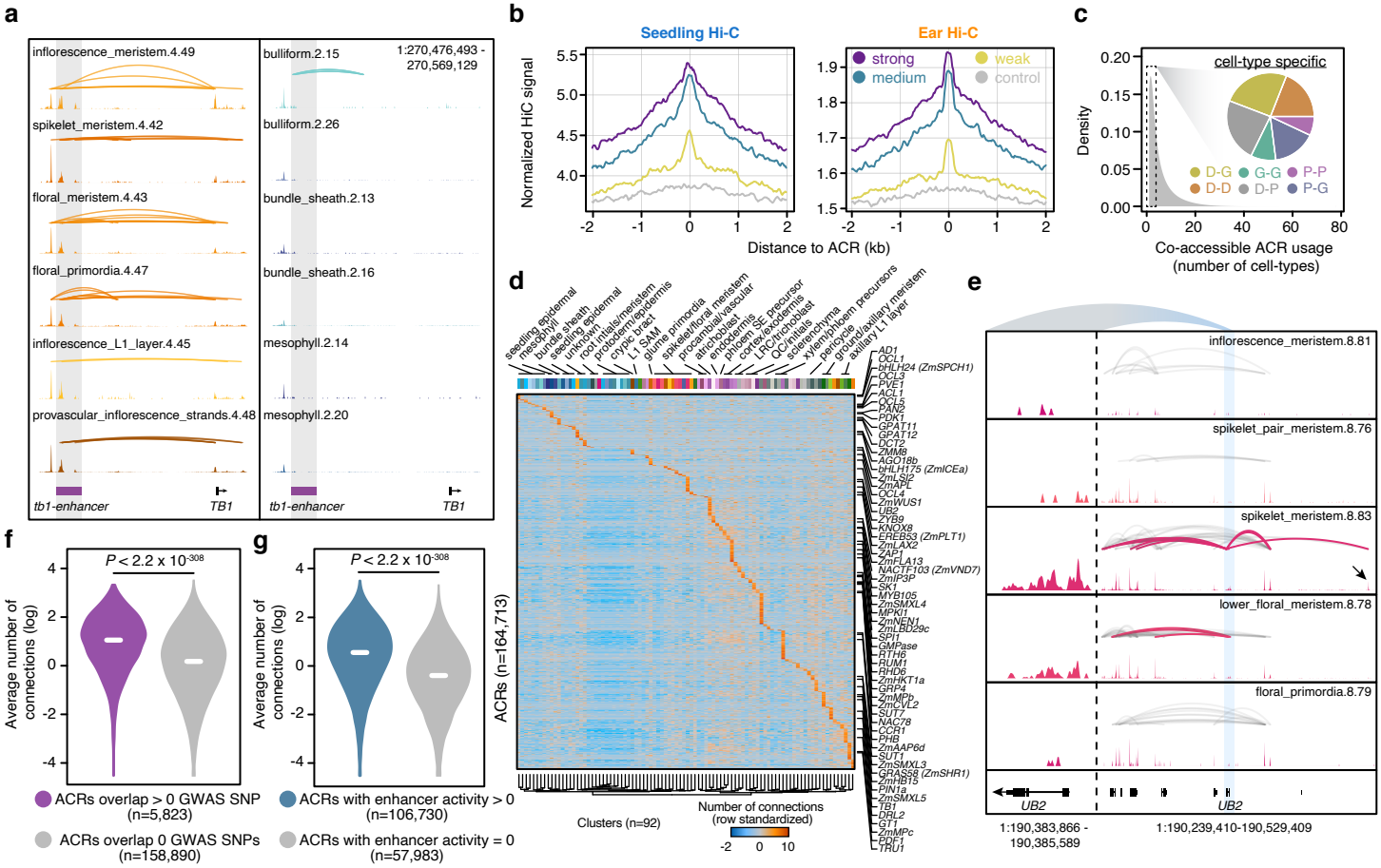

Figure 3: Co-accessible ACRs reflect *in vivo* chromatin interactions and are established by cell-type specific TFs. **a**, Comparison of ear and seedling co-accessible ACRs across nine cell-types at the genetically mapped *tb1-enhancer* domestication locus (highlighted region). Link height reflects co-accessibility scores between ACRs across cells in a cluster. **b**, Average normalized Hi-C signal across 4-kb windows centered on ACRs equally distributed into three groups (each group: n=54,904) based on the number and strength of participating co-accessible links. **c**, Co-accessible ACR interaction frequency across clusters. Inset: Single cell-type co-accessible links (n=1,018,417) for different genomic contexts. **d**, Standardized (row-wise) number of connections for each ACR (rows) by cell-type (columns). Column color map reflect cell-types from the legend in Extended Data Fig. 4. Gene-proximal ACRs for a subset of marker genes are indicated on the right. **e**, Right, chromatin accessibility and co-accessible ACR links surrounding the *UB2* locus associated with ear row number and tassel branch number quantitative traits. Black arrow indicates a distal ACR upstream of *UB2* present only in spikelet meristems. Co-accessible links with an edge within 2-kb of *UB2* are colored pink while remaining links are grey. Link height represents co-accessibility strength. Left, close-up of accessibility profiles of *UB2*. **f**, Distributions of average ACR-ACR links across cell-types for ACRs that overlap (purple) and do not overlap (grey) phenotype-associated genetic variants from maize GWAS. The median of each distribution is shown as a white horizontal line. Violin plots present the entire range of average number of connections on a log scale. Hypothesis testing was conducted within the *R* statistical framework via Wilcoxon rank sum test. **g,** Distributions of average ACR-ACR links celltypes for ACRs with (blue) and without (grey) enhancer activity (log2 RNA/input greater than 0). Hypothesis testing and distribution illustration was performed similarly as panel **f**.

178 predictability of *in vivo* interactions using co-accessible ACRs, we estimated the interaction
179 strength of each ACR by integrating correlative scores across cell-types (Methods). ACRs
180 classified by interaction strength recapitulated expected *in vivo* chromatin interaction frequencies,
181 where even the weakest class of co-accessible ACRs were associated with elevated interaction
182 frequencies relative to flanking and randomized control regions (**Fig. 3b**).

183 Cataloguing the usage of co-accessible ACRs across cell-types identified more than 27%
184 (~1M in total) that were unique to a single type, 49% of which were classified as distal-
185 genic/proximal, with an average of 11,069 distinct links per cell-type (**Fig. 3c**). Consistent with
186 regulatory models where a single gene can interact with multiple distant loci, proximal ACRs,
187 rather than distal or genic ACRs, were associated with the greatest number of links on average
188 (Wilcoxon rank sum test: P < 2.2e-308, **Extended Data Fig. 7c**). Highlighting long-range "hub"
189 interactions as a key contributors towards cell identity, cell-type specific co-accessible ACRs were
190 associated with greater number of links per site (Wilcoxon rank sum test: P < 2.2e-308) and a
191 greater proportion of links involving distal ACRs (Chi-squared test: P < 2.2e-308, **Extended Data**
192 **Fig. 7c, d**). Furthermore, the interactive capacity of any given ACR strongly depended on the cell-
193 type context (**Fig. 3d**). For example, *UNBRANCHED2* (*UB2*) – a major ear row number and tassel
194 branch number quantitative trait locus[29] – demonstrated preferential accessibility in spikelet
195 meristems that coincided with the greatest number of *UB2* proximal to distal ACR interactions,
196 including a cell-type specific ACR located upstream approximately 150-kb (**Fig. 3e**). We posited
197 that ACRs with expanded interactive capacity resemble enhancers with the potential to influence
198 organismal phenotypes. Indeed, ACRs with enhancer activity and co-localization with phenotype-
199 associated genetic variants from GWAS were associated with a significantly greater number of
200 ACR-ACR connections (Wilcoxon rank sum; P < 2.2e-308, **Fig. 3f**, **g**). These results highlight the
201 occurrence of diverse cell-type specific regulatory configurations among distal enhancer ACRs
202 and their target genes and implicate genetic variants perturbing highly interactive distal enhancers
203 as major contributors towards phenotypic variation.

204 The structural protein, CCCTC-binding factor (CTCF) plays an important role in metazoan
205 genome organization and is notably absent in plant lineages[30]. In search of an orthogonal factor
206 in maize, we hypothesized that higher-order chromatin structure captured by co-accessible ACRs
207 may be driven by TFs recognizing similar sequence motifs embedded within interacting
208 accessible regions. Comparison of motif occurrences between co-accessible link edges indicated
209 that ACRs in co-accessible links are more similar to one another than randomly linked ACRs
210 (empirical; P < 1e-4, **Extended Data Fig. 7e**). Furthermore, we identified several cases where
211 co-accessible ACR edges were reciprocally enriched (FDR < 0.05, Methods) for the same TF
212 motif in both cell-type specific and non-specific co-accessible links (**Extended Data Fig. 7f**). We
213 identified *TEOSINTE BRANCHED1/CYCLOIDEA/PROLIFERATING CELL NUCLEAR ANTIGEN*
214 *FACTOR1* (*TCP*), *APETALA2/ETHYLENE-RESPONSIVE ELEMENT BINDING PROTEINS*
215 (*AP2-EREBP*) and *LATERAL ORGAN BOUNDARIES DOMAIN* (*LBD*) motifs that were not only
216 broadly associated with co-accessible edges across cell-types (FDR < 0.05), but also exhibited
217 strikingly similar GC-rich palindromic binding sites (**Extended Data Fig. 7f, g**). A role in chromatin
218 organization is supported by previous research demonstrating *TCP* motif overrepresentation in
219 topologically associated domain-like (TAD) boundaries in *Oryza sativa* and *Marchantia*
220 *polymorpha,* and the distal edges of chromatin loops in *Zea mays*[27,28,31,32].
221
222 **Dynamic chromatin accessibility specifies cell developmental trajectories**
223 The apical domains of maize enclose undifferentiated meristematic stem cells that continuously
224 give rise to all differentiated cell-types[33,34]. To define a *cis*-regulatory catalog of temporal cell-type
225 progressions, we estimated pseudotime scores for ordered nuclei across 18 developmental
226 trajectories reflecting meristematic to differentiated cell-states; identifying ACRs, TF loci, and TF
227 motifs with significant accessibility variation across pseudotime in a given trajectory (**Fig. 4a**,
228 **Extended Data Fig. 8**, **Supplementary Data 3-6**, Methods). To showcase the power of trajectory
229 construction to characterize a relatively understudied process, we focused our analysis on root

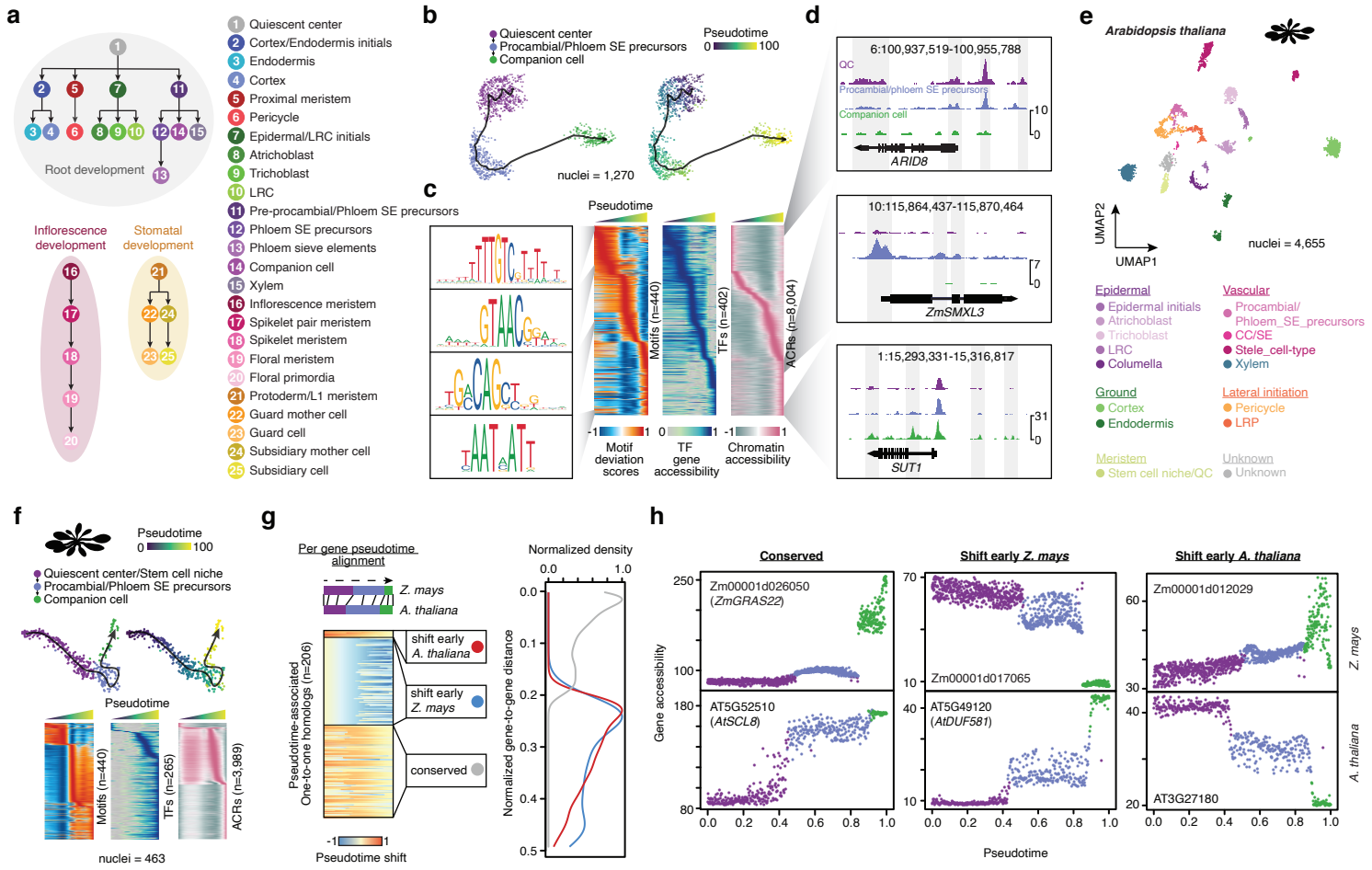

Figure 4: Chromatin accessibility is dynamic across pseudotime and conserved between *Arabidopsis thaliana* and *Zea mays*

a, Overview of pseudotime trajectory analysis. Inflorescence development was performed for both pistillate and staminate inflorescence. **b,** UMAP embedding of companion cell developmental trajectory depicting cell-types (left) and pseudotime progression (right). **c,** Relative motif deviations for 440 TF motifs (left, rows), 402 TF gene accessibility scores (middle, rows), and relative accessibility of 8,094 ACRs (right, rows) associated with pseudotime (columns). Four motifs enriched along the trajectory gradient are shown on the left. ACRs, accessible chromatin regions; TF, transcription factor. **d,** Genome browser screenshots of cell-type specific chromatin accessibility profiles along the developmental trajectory for quiescent center, procambial/phloem sieve element precursor, and companion cell at associated marker gene loci. **e,** UMAP embedding based on whole-genome chromatin accessibility profiles of 4,655 *Arabidopsis thaliana* root nuclei. **f,** UMAP embedding of compnaion cell developmental trajectories in *Arabidopsis thaliana* depecting cell-types (left) and pseudotime progression (right). Motifs, TFs, and ACRs with significant association with pseudotime are shown as heatmaps below. **g,** Per-gene pseudotime shift scores from alignments between *Zea mays* and *Arabidopsis thaliana* companion cell development progressions, clustered by k-means into three groups. Distribution of gene-gene distances from the alignments are shown on the right, split by k-mean groups. **h,** Exemplary one-to-one homologs between *Arabidopsis thaliana* and *Zea mays* for the three groups split by pseudotime shifts. Acronyms: CC, compansion cell; LRC, lateral root cap; LRP, lateral root primordia. QC, quiescent center; SE, sieve elements.

230 phloem companion cell (PCC) development (**Fig. 4b**). Ordering nuclei along the PCC trajectory,
231 we identified 8,004 ACRs, 440 TF motifs, 7,955 genes, and 402 TF loci that were differentially
232 accessible across pseudotime (**Fig. 4c**, Methods). Several known meristem and phloem
233 developmental genes including *AT-RICH INTERACTIVE DOMAIN-CONTAINING 8* (*ARID8*)[35],
234 *SUPPRESSOR OF MAX2 1-LIKE3* (*ZmSMXL3*)[36], *and SUCROSE TRANSPORTER 1*
235 (*ZmSUT1*)[37], were identified among the top differentially accessible genes throughout PCC
236 development (**Fig. 4d**). To realize conserved regulatory mechanisms in plant root development,
237 we profiled chromatin accessibility in 4,655 nuclei from 7-day old embryonic root tissues in the
238 eudicot model species *Arabidopsis thaliana* and constructed eight pseudotime trajectories
239 encompassing vascular, dermal and ground development (**Fig. 4e, f, Extended Data Fig. 9,**
240 **Supplementary Data 7-11**). Maintaining focus on PCC development, we aligned *Z. mays* and *A.*
241 *thaliana* trajectories using a time-warping algorithm. Consistent with recent comparative analysis
242 of vascular development in *O. sativa*, *A. thaliana,* and *Solanum lycopersicum*[38], only 206 out of
243 10,976 putative orthologs were significantly associated (FDR < 0.01) with PCC pseudotime in
244 both species, indicating that the majority PCC trajectories-associated genes are unique to each
245 lineage (97% *Z. mays*, 83% *A. thaliana*). However, of the 206 PCC-associated orthologs, ~50%
246 (102/206) exhibited similar patterns of gene accessibility across pseudotime (**Fig. 4g**, **Extended**
247 **Data Fig. 10a, b**). Several putative orthologs with matching gene accessibility patterns have been
248 previously associated with PCC development, such as *SCARECROW-LIKE8* (*SCL8*), which
249 displays an increasing expression gradient in nascent to mature *A. thaliana* PCCs in a previously
250 generated *A. thaliana* root cell-type gene expression atlas (**Fig. 4h**)[39]. Despite evolutionary
251 conserved sequence homology, the remaining homologs (n=104) exhibited differential
252 accessibility patterns clustered into two groups that reflect changes in the timing of gene
253 accessibility across PCC development, underscoring functional novelty in PCC development
254 between *Z. mays* and *A. thaliana*. To understand the extent of innovation in *cis* regulation along

255 the pseudotime continuum, we aligned *Z. mays* and *A. thaliana* TF motif accessibility profiles
256 associated with PCC progression (**Extended Data Fig. 10c**). Of the 440 motifs, 142 demonstrated
257 highly conserved *cis*-regulatory dynamics between species (**Extended Data Fig. 10d, e**). Indeed,
258 TFs recognizing the top four motifs ranked by normalized distances (Methods) included
259 *HOMEOBOX25* (*HB25*), *HOMEOBOX18* (*HB18*), *NAC DOMAIN CONTAINING PROTEIN 55*
260 (*NAC055*), and *NAC DOMAIN CONTAINING PROTEIN 83* (*NAC083*) that have been previously
261 implicated in regulation of hormonal responses and vascular development[40-42]. Gene expression
262 profiles of these TFs from published root cell-type resolved data in *A. thaliana* was largely
263 restricted to maturing procambial and companion cells, consistent with motif accessibility
264 dynamics in both *Z. mays* and *A. thaliana* ontogenies (**Extended Data Fig. 10f-h**)[39].
265 In summary, we describe 92 distinct cell-states from a suite of *Z. mays* organs, many of
266 which previously lacked prior genome-wide characterization. We provide evidence supported by
267 RNA *in situ* hybridization for the use of chromatin accessibility as a robust proxy of gene
268 expression. We defined the TFs, CREs, and other genomic regions that discretize cell-type
269 identities and the sequential trajectories for an array of developmental ontogenies. We
270 demonstrate that floral cell-type specific ACRs have been the historical targets of modern
271 agronomic selection and while subject to considerable sequence constraint within maize, cell-
272 type specific ACRs harbor polymorphisms associated with significant phenotypic variation. By
273 considering patterns of gene and motif accessibility across two highly diverged species, our
274 results indicate that a majority of genes involved in cell-type development are unique to each
275 lineage. This finding contrasts with greater conservation of *cis*-regulatory dynamics, as a greater
276 proportion of TF motifs exhibited consistent spatiotemporal progressions. Lastly, we anticipate
277 that the dissemination of ACRs by cell-type presents an ideal framework for future crop
278 improvement efforts via genome editing and synthetic biology approaches.
279
280

ACKNOWLEDGEMENTS

We would like to acknowledge Dr. Zefu Lu for training in nuclei extraction, Julie Nelson from the University of Georgia flow cytometry core for helping sort nuclei, Noah Workman and Julia Portocarrero from the Georgia Genomics and Bioinformatics Core for library preparation, the Georgia Advanced Computing Resource Center for providing access to computing resources, and Tyler Earp for assistance with data management. This study was funded by support from the National Science Foundation (IOS-1856627 and IOS-1802848), the Pew Charitable Trusts and the UGA Office of Research to RJS, the National Science Foundation (IOS-1916804) to AG, and an NSF Postdoctoral Fellowship in Biology (DBI-1905869) to APM. AG and RJS are also supported by an NSF Collaborative award to support this research (IOS-2026554 and IOS-2026561). RJS is a Pew Scholar in the Biomedical Sciences, supported by The Pew Charitable Trusts.

AUTHOR CONTRIBUTIONS

APM and RJS designed the research. APM and ZC performed the experiments. APM, ZC, AG and RSJ analyzed the data. APM and RJS wrote the manuscript.

COMPETING INTERESTS

RJS is a co-founder of REqest Genomics, LLC, a company that provides epigenomic services. APM, ZC and AG declare no competing interests.

SUPPLEMENTARY INFORMATION

Supplementary information is available for this paper.

CORRESPONDENCE

Correspondence and requests for materials should be addressed to Robert J. Schmitz (schmitz@uga.edu) and Alexandre P. Marand (marand@uga.edu).

332 **METHODS**

333 **Plant material and growth conditions**

334 For libraries derived from seedlings, kernels from genotypes B73 and Mo17 were obtained from
335 USDA National Plant Germplasm System (https://npgsweb.ars-grin.gov) and sown in Sungro
336 Horticulture professional growing mix (Sungro Horticulture Canada Ltd.). Soil was saturated with
337 tap water and placed under a 50/50 mixture of 4100K (Sylvania Supersaver Cool White Delux
338 F34CWX/SS, 34W) and 3000K (GE Ecolux w/ starcoat, F40CX30ECO, 40W) lighting. Seedlings
339 were grown under a photoperiod of 16 hours of light, eight hours of dark. The temperature was
340 approximately 25°C during light hours with a relative humidity of approximately 54%. Above
341 ground seedling tissues were harvested between 8 and 9 AM six days (V1-stage) after sowing.
342 We used both fresh (B73/Mo17 pooled) and flash frozen (B73 only) seedling tissue to construct
343 scATAC-seq libraries (**Supplementary Table 1**).

344 Maize root samples were obtained as follows: B73 kernels were sterilized with 70% EtOH
345 treatment for 5 minutes. After removing the ethanol solution, kernels were suspended with 50%
346 bleach for 30 minutes, followed by five washes with autoclaved Milli-Q water. Sterilized kernels
347 were then sown onto mesh plates with half strength MS (Phytotech laboratories, catalog: M519)
348 media and wrapped in Millipore tape. Plates were incubated in a Percival growth chamber with a
349 photoperiod of 16 hours of light, eight hours of dark. The growth chamber temperature was set to
350 25°C with a relative humidity of approximately 60%. Apical root tips (bottom 2 cm) of seminal and
351 primary root samples were harvested six days (V1-stage) after sowing between 8 and 9 am.
352 Crown root samples (21 days after sowing) were derived from the three developmental zones of
353 greenhouse grown B73 plants between 8 and 9 am and rinsed with sterile water 3 times.

354 Data generated from young inflorescence (ear and tassel primordia) were derived from
355 B73 maize grown in the greenhouse. Inflorescence primordia were extracted from shoots
356 harvested approximately one month (V7-stage, 2-4 mm) after sowing, between 8 and 9 AM.
357 Inflorescence primordia between three and eight millimeters from the base to the apical tip were

358 placed in sterile water and used for nuclei isolation. Axillary buds (~30 samples per library) were
359 taken from B73 maize plants grown in the greenhouse at approximately the same developmental
360 stage (V7) as tassel and ear primordia.
361
362 **Single cell ATAC-seq library preparation**
363 Each library was prepared by mixing at least three independent biological samples (3-4 seedlings,
364 3 tassel or ear primordia, 12-14 root tips, 12-14 crown root samples and ~30 axillary buds). One
365 scATAC-seq library (B73 seedling) was derived from flash frozen tissue (liquid nitrogen, followed
366 by 7-day -80°C storage), while the remaining nine libraries were constructed with freshly
367 harvested tissue (**Supplementary Table 1**).
368 To isolate individual plant nuclei, fresh or flash frozen tissue from multiple biological
369 samples were placed on petri dishes and vigorous chopped with a razor blade for two minutes in
370 ~500 uL LB01 buffer (15mM Tris pH 7.5, 2mM EDTA, 0.5mM Spermine, 80mM KCl, 20mM NaCl,
371 15mM 2-ME, 0.15% TrixtonX-100). Homogenized tissue was then filtered through two layers of
372 miracloth, stained with DAPI to a final concentration of ~1uM and loaded onto a Beckman Coulter
373 MoFlo XDP flow cytometer instrument. A total of 120,000 nuclei were sorted for each sample
374 across four catch tubes (30,000 nuclei each) containing 200 uL LB01. Isolated nuclei were spun
375 down in a swinging-bucket (5 minutes, 500 rcf) centrifuge resuspended in 10uL LB01, pooled,
376 and then visualized on a hemocytometer with a fluorescent microscope. Nuclei suspensions were
377 then spun down (5 minutes, 500 rcf) and resuspended in diluted nuclei buffer (10X Genomics) to
378 a final concentration of 3,200 nuclei per uL and used as input for scATAC-seq library preparation
379 (5 uL; 16,000 nuclei total). Samples were kept on ice for all intermittent steps. For B73/Mo17
380 mixed library, we pooled 8,000 nuclei from both B73 and Mo17 that were independently isolated.
381 Single-cell ATAC-seq libraries were constructed according to the manufacture's instruction (10X
382 Genomics, catalog: 1000176). Libraries were sequenced with Illumina NovaSeq 6000 in dual-
383 index mode with six and 16 cycles for i7 and i5 index, respectively.

384

385 ***In situ* hybridizations**

386 3-4mm tassel and ear primordia and young seedlings from the maize B73 inbred line were
387 dissected and fixed in a cold paraformaldehyde acetic acid solution (4% PFA) for 48 hours.
388 Following dehydration through a graded ethanol series and clearing of the tissue with a Histo-
389 clear II solution (Electron Microscopy Sciences), samples were embedded using Paraplast Plus
390 tissue embedding media (McCormick Scientific). 8mm sections were hybridized at 56°C with
391 antisense probes labelled with digoxigenin (DIG RNA labeling mix, Roche), and detected using
392 NBT/BCIP (Roche). Probes were synthesized by *in vitro* transcription (T7 RNA polymerase,
393 Promega) of PCR products obtained from embryo cDNA or from digested full-length cDNA clones.
394 The vectors and primers used for probe design are listed in **Supplementary Table 6**.

395

396 **Raw reads processing**

397 The following data processing was performed using each tissue and/or replicate independently
398 unless noted otherwise. Raw BCL files were demultiplexed and convert into fastq format using
399 the default settings of the 10X Genomics tool *cellranger-atac makefastq* (v1.2.0). Partial raw read
400 processing (adapter/quality trimming, mapping and barcode attachment/correction) was carried
401 out with *cellranger-atac count* (v1.2.0) using AGPv4 of the maize B73 reference genome[43].
402 Properly paired, uniquely mapped reads with mapping quality greater than 10 were retained using
403 *samtools view* (v1.6; -f 3 -q 10) and by filtering reads with XA tags[44]. Duplicate fragments were
404 collapsed on a per-nucleus basis using *picardtools* (http://broadinstitute.github.io/picard)
405 *MarkDuplicates* (v2.16; BARCODE_TAG=CB REMOVE_DUPLICATES=TRUE). Reads mapping
406 to mitochondrial and chloroplast genomes were counted for each barcode, then excluded from
407 downstream analysis. We removed reads representing potential artifacts by excluding alignments
408 coincident with a blacklist of regions composed of low-complexity and homopolymeric sequences
409 (*RepeatMasker* v4.07)[45], nuclear sequences with homology (greater than 80% identity and

410 coverage) to mitochondrial and chloroplast genomes (*BLAST*+ v2.7.1)[46], regions exhibiting Tn5
411 integration bias from Tn5-treated genomic DNA (1-kb windows with greater than 2-fold coverage
412 over the genome-wide median), and potential collapsed sequences in the reference (1-kb
413 windows with greater than 2-fold coverage over the genome-wide median using ChIP-seq input).
414 Genomic Tn5 and ChIP input data were acquired from Ricci, Lu and Ji et al[10]. BAM alignments
415 were then converted to single base-pair Tn5 integration sites in BED format by adjusting
416 coordinates of reads mapping to positive and negative strands by +4 and -5, respectively, and
417 retaining only unique Tn5 integration sites for each distinct barcode. Sequencing saturation was
418 calculated as the proportion of unique reads relative to the estimated library complexity output by
419 the *MarkDuplicates* function apart of picardtools.
420
421 **Cell calling**
422 To identify high-quality nuclei (a term used interchangeably with "barcodes") using the filtered set
423 of alignments, we implemented heuristic cutoffs for genomic context and sequencing depth
424 indicative of high-quality nuclei. Specifically, we fit a smoothed spline to the $\log_{10}$ transformed
425 unique Tn5 integration sites per nucleus (response) against the ordered $\log_{10}$ barcode rank
426 (decreasing per-nucleus unique Tn5 integration site counts) using the *smooth.spline* function
427 (spar=0.01) from base R[47]. We then used the fitted values from the smoothed spline model to
428 estimate the first derivative (slope), taking the local minima within the first 16,000 barcodes as a
429 potential knee/inflection point (16,000 was selected to match the maximum number of input
430 nuclei). We set the unique Tn5 library depth threshold to the lesser of 1,000 reads and the
431 knee/inflection point, excluding all barcodes below the threshold. Spurious integration patterns
432 throughout the genome can be representative of incomplete Tn5 integration, fragmented/low-
433 quality nuclei, or poor sequence recovery, among other sources of technical noise. In contrast,
434 high quality nuclei often demonstrate a strong aggregate accessibility signal near TSSs.
435 Therefore, we implemented two approaches for estimating signal-noise ratios in our scATAC-seq

436 data. First, nuclei below two standard deviations from the mean fraction of reads mapping to within
437 2-kb of TSSs were removed on a per-library basis. Then, we estimated TSS enrichment scores
438 by calculating the average per-bp coverage of 2-kb windows surrounding TSSs, scaling by the
439 average per-bp coverage of the first and last 100-bp in the window (background estimate; average
440 of 1-100-bp and 1901-2000-bp), and smoothing the scaled signal with rolling-means (R package;
441 *Zoo*). Per barcode TSS enrichment scores were taken as the maximum signal within 250-bp of
442 the TSS. Lastly, for each library, we removed any barcode with a proportion of reads mapping to
443 chloroplast and mitochondrial genomes greater than two standard deviations from the mean of
444 the library.
445
446 **Detection of multiplet droplets**
447 To estimate the empirical proportion of doublets present in our data, we demultiplexed the two-
448 genotype (B73 and Mo17) pooled seedling scATAC-seq sample and assessed the proportion of
449 barcodes reflecting a mixtures of reads derived from both genotypes. Specifically, B73 and Mo17
450 whole genome short read resequencing data were acquired from PRJNA338953. Paired-end
451 reads were quality and adapter trimmed with *fastp* (v0.19.5)[48] and aligned to the B73 v4 maize
452 reference genome[43] using *BWA mem*[49] with non-default settings (-MT 1). Duplicate reads were
453 removed using *samtools rmdup*[44] (v1.6). The genomic coordinates of short nucleotide variants
454 (SNVs; single nucleotide polymorphisms [SNPs] and small insertions/deletions [INDELs]) for both
455 genotypes were identified using *freebayes*[50] (v1.0.0) with non-default settings (--min-repeat-
456 entropy 1 --min-alternate-fraction 0.05). Only biallelic SNPs – requiring at least 5 reads per
457 genotype where B73 and Mo17 were homozygous for reference and alternate nucleotides,
458 respectively – were retained. Genotypes were called by modeling allele counts as a binomial
459 distribution with a term accounting for the sequencing error rate, E_t (determined empirically as
460 the fraction of SNPs failing to match either allele), estimating posterior probabilities via Bayes

461 theorem, and assigning the genotype (or mixture of genotypes) with the greatest probability (Eq.
462 1-7). Specifically, the probability to observe k out of n SNPs from B73 can be modeled as a
463 binomial distribution for each B73 (A_l), Mo17 (A_2), and doublet barcode state (N) (Eq. 1-3):
464
465 1. $P(k|A_1) = \binom{n}{k} \times {E_t}^{n-k} \times (1 - E_t)^k$
466
467 2. $P(k|A_2) = \binom{n}{k} \times (1 - E_t)^{n-k} \times {E_t}^{k}$
468
469 3. $P(k|N) = \binom{n}{k} \times (0.5)^k \times (0.5)^{n-k}$
470
471 Let $P(A_1|k)$, $P(A_2|k)$, and $P(N|k)$ reflect posterior probabilities for genotypes B73, Mo17, and
472 doublet barcodes given k allele counts from B73; posterior probabilities can be estimated as
473 follows (Eq. 4-6):
474
475 4. $P(A_1|k) = \frac{P(k|A_1) \times P(A_1)}{\sum_{i=0}^{n} P(k|A_i) \times P(A_i)}$
476
477 5. $P(A_2|k) = \frac{P(k|A_2) \times P(A_2)}{\sum_{i=0}^{n} P(k|A_i) \times P(A_i)}$
478
479 6. $P(N|k) = \frac{P(k|N) \times P(N)}{\sum_{i=0}^{n} P(k|A_i) \times P(A_i)}$
480
481 Finally, the genotype called for each barcode was determined as the event with the greatest
482 posterior probability (Eq. 7):
483
484 7. $\max\{P(A_1|k), P(A_2|k), P(N|k)\}$

485

486 ***In-silico* sorting**

487 To provide sufficient sensitivity for peak calling prior to clustering, we followed an *in-silico* sorting
488 strategy to identify crude clusters of similar cells within each organ[1]. To do so, we generate a
489 binary matrix representing the presence/absence of Tn5 integration sites in 1-kb windows across
490 all cells in a given organ. Bins with less than 1% accessible cells and cells with less than 100
491 accessible bins were removed. This binary matrix was then transformed using the matrix
492 normalization method term-frequency inverse document-frequency (TF-IDF). Briefly, the TF term
493 was estimated by weighting binary counts at each bin by the total number of bins containing Tn5
494 integration sites in a given cell, scaling each cell to sum to 100,000, adding a pseudo-count of
495 one, and log transforming the resulting values to reduce the effects of outliers in downstream
496 processing. The IDF term was calculated as the log transformed ratio of the total number of nuclei
497 to the number of nuclei that were marked as accessible for a given bin. We add a pseudo-count
498 of one to the inverse frequency term to avoid taking the log of zero. The TF-IDF scaled matrix
499 was estimated by taking the dot product of the TF and IDF matrices. To enable faster downstream
500 computation, we kept the top 25,000 bins with the greatest TF-IDF variance across nuclei. The
501 reduced TF-IDF matrix was denoised with singular value decomposition (SVD), retaining the 2nd
502 – 11th dimensions (termed Latent Sematic Indexing, LSI). Each row was centered and
503 standardized, capping the values at $\pm$ 1.5. Crude clusters were visually identified (k=[6..12]) using
504 ward.D2 hierarchical bi-clustering on the cosine distances of LSI nuclei and bin embeddings.

505

506 **ACR identification**

507 ACRs were identified by treating each bulk and single-cell ATAC-seq library as a traditional bulk
508 ATAC-seq library. Aligned reads were filtered by mapping quality greater than 10, and duplicate
509 reads were removed via *samtools rmdup.* We then identified ACRs for each library by converting
510 the BAM alignments in BED format, adjusting the coordinates to reflect single-base Tn5

511 integrations, and running *MACS2*[51] with non-default parameters: --extsize 150 --shift -75 --
512 nomodel --keep-dup all. A final set of ACRs for comparing bulk and aggregate scATAC-seq
513 libraries (**Extended Data Fig. 1b**) was constructed by taking the union of ACRs across all
514 libraries. To leverage the increased sensitivity afforded by cell-type resolved cluster information
515 while ensuring robust reproducibility in ACR identification, we generated pseudo-replicated bulk
516 alignments using the LSI-based crude clusters (see above, "*In-silico* sorting"). Pseudo-replicates
517 were constructed by randomly allocating nuclei from each cluster into two groups, with a third
518 group composed of all cells from the cluster (cluster bulk). These groupings were used to
519 concatenate Tn5 integration sites corresponding to the nuclei from each group into three BED
520 files. ACRs were then identified from the enrichment of Tn5 integration sites from the pseudo-
521 replicate or cluster bulk aggregates using *MACS2* run with non-default parameters: --extsize 150
522 --shift -75 --nomodel --keep-dup all. ACRs from both pseudo-replicates and the cluster bulk were
523 intersected with BEDtools, retaining ACRs on the conditional intersection of all three groupings
524 (both pseudo-replicates and the cluster bulk) by at least 25% overlap. The remaining ACRs were
525 then redefined as 500-bp windows centered on the ACR coverage summit. To integrate
526 information across all clusters, ACRs from each cluster were concatenated into a single master
527 list. Lastly, overlapping ACRs were filtered recursively to retain the ACR with the greater
528 normalized kernel Tn5 integration density as previously described[25].
529

530 **Nuclei clustering**

531 Starting with a binary nucleus x ACR matrix, we first removed ACRs that were accessible in less
532 than 0.5% of all nuclei, and filtered nuclei less than 50 accessible ACRs. Inspired by recent
533 developments in modeling single-cell RNA-seq data[52], we developed a regularized quasibinomial
534 logistic framework that overcomes noise inherent to sparse, binary scATAC-seq data by pooling
535 information across ACRs while simultaneously removing variation due to technical effects,
536 particularly those stemming from differences in barcode sequencing depths. First, a subset of

537 5,000 representative ACRs selected by kernel density sampling of ACR usage (fraction nuclei
538 that are accessible at a given ACR) were used to model the parameters of each ACR, using ACR
539 usage as a covariate in a generalized linear model. Specifically, the expected accessibility of an
540 ACR, y_i, can be estimated with a generalized linear model containing a binomial error distribution
541 and logit-link function, and an overdispersion term with a quasibinomial probability density
542 function (Eq. 8).
543
544 8. $\mathbb{E}(\mathrm{y}_i) \sim \beta_0 + \beta_1 log10(t)$
545
546 Where t is a vector of the sums of accessible ACRs across cell j (Eq. 9):
547
548 9. $t = \sum_i \mathrm{y}_{ij}$
549
550 To prevent over-fitting and ensure robust estimates in light of sampling noise, we learned the
551 global regularized model parameters, including overdispersion, using the representative ACRs by
552 fitting each parameter against the $\log_{10}$ fraction of accessible nuclei via kernel regression,
553 resulting in smoothed parameter estimates across the spectrum of ACR accessibility penetrance
554 present in these data. The learned global regularized model parameters were then used to
555 constrain fitted values across all ACRs for each nucleus with a simple affine transformation. To
556 account for technical variation among nuclei (variation in barcode $\log_{10}$ transformed read-depth,
557 in particular) we calculated Pearson residuals for each ACR, scaling the residuals by the
558 regularized dispersion estimate and centering values via mean subtraction, representing
559 variance-stabilized and read-depth normalized values of accessibility for a nucleus at a given
560 ACR. We note that this method is amenable to calculating residuals that account for additional

561 sources of technical variation, including categorical and numeric covariates, that may obscure
562 biological signal, such as batch effects, proportion of mitochondrial reads, etc.

563 The dimensionality of the Pearson residual matrix was reduced using singular value
564 decomposition (SVD) implemented by the R package *irlba*[53], retaining the first 25 left singular
565 vectors scaled by singular values (hereafter referred to as nuclei embeddings), analogous to
566 principal components (PCs) on an uncentered matrix. Nuclei embeddings were then standardized
567 across components and filtered to remove components correlated with barcode read depth
568 (Spearman's rho > 0.7). We further reduced the dimensionality of the nuclei embedding with
569 Uniform Manifold Approximation Projection (UMAP) via the R implementation of *umap-learn*
570 (min_dist = 0.1, k=50, metric="euclidean"). Nuclei were clustered with the *Seurat* v3[54] framework
571 and Louvain clustering on a k=50 nearest neighborhood graph at a resolution of 0.02 with 100
572 iterations and 100 random starts. Clusters with aggregated read depths less than 1.5M were
573 removed. To filter outliers in the UMAP embedding, we estimated the mean distance for each
574 nucleus with its *k* (*k*=50) nearest neighbors and removed nuclei greater than 3 standard deviations
575 from the mean.

576 We observed fine-scale heterogeneity within major clusters, thus we repeated our
577 clustering pipeline for each major cluster independently by partitioning the SVD embedding into
578 the top 20 components, L2 normalizing nuclei embeddings across components, and projecting
579 the L2-normalized embeddings into the UMAP space. Subclusters of nuclei were identified by
580 Louvain clustering on the L2 normalized SVD embedding (resolution set manually, range = 0.6 –
581 1.0) with 20 nearest neighbors, filtering outlier nuclei more than 2 standard deviations from the
582 mean distance of 25 nearest neighbors within each cluster.

583 For analysis of chromatin accessibility across clusters, we assembled a matrix of clusters
584 by ACRs by aggregating the number of single-base resolution Tn5 integration sites from nuclei
585 within the same cluster for each ACR, analogous to normalizing by the proportion of reads in
586 peaks for each cluster. To account for differences in read depth and other technical factors, the

587 raw counts were transformed with *edgeR's* "cpm" (log=T, prior.count=5) as previously
588 described[55]. Log-transformed ACR coverage scores were quantile normalized using
589 "normalize.quantiles" with the R package, *preprocessCore.* Finally, to aid data visualization, we
590 estimated per ACR Z-scores across clusters by mean subtraction and standardization (identical
591 to row-wise execution of the R function, "scale").
592
593 **Identification of co-accessible ACRs**
594 Recent experiments of population-level chromatin accessibility found that pairwise correlations of
595 accessibility among ACRs recapitulates higher-order chromatin interactions observed in Hi-C and
596 other chromatin architecture experiments[24]. A similar framework was applied to populations of
597 single cells, which showed that co-accessible ACRs are typically more conserved and functionally
598 associated[26]. To identify potentially functional co-accessible ACRs, we applied a recently
599 developed method, *Cicero*[23], that estimates regularized correlation scores (ranging from -1 to 1)
600 among nearby ACRs with graphical LASSO to penalize potential interactions by physical
601 distances. Using the binary nuclei x ACR matrix as input, we subset nuclei by their subcluster IDs
602 and estimated co-accessibility among ACRs within 500-kb for each of the 92 clusters,
603 independently. *Cicero* was run by applying a background sample of 100 random regions, and 15
604 nuclei pseudo-aggregates based on k-nearest-neighbors derived from the UMAP coordinates. To
605 control the false discovery rate (FDR) of co-accessible ACR calls, we shuffled the nuclei x ACR
606 matrix such that the total number of reads per ACR and reads per nucleus were identical to the
607 original matrix. We then repeated co-accessible ACR identification with the shuffled matrix,
608 keeping the original parameters to *Cicero* unchanged. Empirical FDR cluster-specific cut-offs
609 were constructed by identifying the minimum positive co-accessibility score in the background
610 where the FDR < 0.05. Co-accessible links below cluster-specific thresholds were removed. Co-
611 accessible ACRs passing thresholds were compared with previously published HiC and HiChIP
612 data sets derived from maize seedling and pistillate inflorescence primordia[10].

613

614 **Estimation of gene accessibility scores**

615 Chromatin accessibility at TSSs and gene bodies exhibit marked correlation with transcription
616 output in bulk samples (**Extended Data Fig. 3f**). To aid the identification of marker genes
617 underlying distinct cell-types, we used *Cicero* to estimate gene activity scores. *Cicero* models
618 gene activity as a weighted accessibility score that integrates both proximal and distal regulatory
619 elements linked to a single gene by co-accessibility analysis (see above section "Identification of
620 co-accessible ACRs"). Relative gene accessibility scores per nucleus were estimated by taking a
621 weighted average (3:1, gene body score to proximal/distal activity) of the scaled number of reads
622 mapping to gene bodies for each barcode (summing to 1) with the *Cicero* estimate of gene activity
623 derived from ACRs mapping to 1-kb upstream of gene TSSs and their associated distal ACRs
624 linked by co-accessible ACRs passing FDR < 0.05 thresholds (connected ACRs were constrained
625 to a minimum and maximum intervening distance of 1- and 500-kb, respectively). These weighted
626 gene accessibility scores were rescaled such that gene accessibility scores for a given nucleus
627 summed to 1.

628 Relative gene accessibility scores exhibited a bimodal distribution with relative gene
629 accessibility values near zero resembling low or non-expressed genes. We applied a gaussian
630 mixture-model (two distributions) based scaling step per cluster to reduce noise introduced by
631 genes with low gene accessibility. Briefly, the average gene accessibility across nuclei was fit to
632 a two distribution gaussian mixture model in each cluster using the R package *mclust*. We
633 estimated cluster-specific scaling parameters determined as the 5% quantile of non-zero gene
634 accessibility values of genes from the gaussian distribution with the larger mean, for each cluster.
635 This parameter was then used to scale gene accessibility scores for all genes in each nucleus
636 within the cluster. Scaled gene accessibility scores were rounded to the nearest integer and
637 normalized across all nuclei and clusters using nucleus-specific size factors estimated as the total
638 gene accessibility of a nucleus divided by the exponential of the mean of log-transformed gene

639 accessibility sums across nuclei. To aid visualization, we smoothed normalized gene accessibility
640 scores by estimating a diffusion nearest neighbor graph (k=15) using the SVD embedding with 3
641 steps similar to the *run_MAGIC* function in R package *snapATAC*[56]. Downstream analyzes based
642 on binarized gene accessibly were conducted by simply converting normalized (non-smoothed)
643 accessibility scores to 1 for all positive values.
644
645 **Cell-type annotation**
646 To identify and annotate cell-types for each barcode, we identified marker genes known to localize
647 to discrete cell-types or domains expected in the sampled tissues/organs based on extensive
648 review of the literature (**Supplementary Table 2**). To enable gene accessibility comparisons
649 among clusters, we generated three pseudo-replicates for each cluster by resampling nuclei
650 within the cluster such that all cluster pseudo-replicates contained the mean number of nuclei
651 across clusters (number of nuclei per pseudo-replicate = 552) without replacement when possible.
652 To identify genes with increased accessibly relative to other clusters, we constructed a reference
653 panel with three pseudo-replicates by uniformly sampling nuclei without replacement from each
654 organ (number of nuclei per organ = 92), with a total of 552 nuclei per reference panel pseudo-
655 replicate. Read counts per gene were summed across nuclei within each pseudo-replicate. Using
656 the *DESeq2* R package, we identified genes with significantly different (FDR < 0.01) accessibility
657 profiles between each cluster and the reference panel.
658 The list of significantly differentially accessible genes was filtered to retain the genes on
659 our list of cell-type specific markers. We initially ranked the top three marker genes in each cluster
660 by their test statistics. To account for clusters containing small proportions of contaminating nuclei
661 of a different cell-type, we adjusted the test statistics using a previously described method[1],
662 effectively scaling marker activity scores by the proportion of nuclei in the cluster that were derived
663 from an organ in which the marker gene i is an expected cell-type. Clusters where the top three
664 markers corresponded to the same cell-type were annotated with the consensus cell-type.

665 As an independent method for cell-type annotation, we devised a resampling and
666 normalization procedure on the $\log_2$ fold-change values of marker genes to evaluate cell-type
667 enrichment across all possible cell-types for each cluster, normalizing enrichment scores by
668 random permutations accounting for different numbers of markers associated with each cell-type.
669 Briefly, starting with differential gene accessibility information for each cluster, we iterated over all
670 cell-types, extracting markers associated with the cell-type of interest. Then, we summed the $\log_2$
671 fold-changes values of all markers and multiplied the sum by the proportion of markers passing
672 heuristic thresholds (fold-change > 2 and FDR < 0.01). This score was subtracted by the average
673 of 1,000 random permuted scores from combinations of markers from the remaining cell-types
674 (selecting the same number of random genes as the cell-type of interest) and divided by the
675 standard deviation of the permuted scores. Cell-type enrichment scores in each cluster were
676 scaled from zero to one by dividing each cell-type enrichment score by the maximum scores
677 across possible cell-types. This approach is effective in normalizing differences arising from
678 varying numbers of markers specified for each cell-type. Additionally, cell-type annotation scores
679 for clusters with mixed or unknown identity are approximately equally distributed, thus controlling
680 ascertainment bias stemming from marker gene selection. Stated differently, an advantage of this
681 approach is that clusters corresponding to cell-types with few or no markers in the tested list are
682 left unassigned as their enrichment scores do not deviated significantly from background levels.
683 Finally, scaled cell-type enrichment scores greater than 0.9 were taken as possible annotations
684 and intersected with putative cell-type labels from the marker ranking approach described above.
685 For clusters with ambiguous marker gene labels, we developed a logistic regression
686 classifier to identify putative cell-types based on whole-genome gene accessibility scores of well-
687 annotated cells. First, we counted the number of Tn5 integration sites per cell overlapping 2-kb
688 upstream to 500-bp downstream of each gene. Read counts were transformed by trimmed mean
689 of M-values (TMM) to enable intra and inter-nucleus comparisons using *edgeR*[57], scaling gene
690 accessibility scores in each nucleus with counts per million. Next, we estimated cell-type

691 enrichment scores for each nucleus by calculating the mean accessibility scores of markers for a
692 given cell-type, subtracting the mean background signal defined as 1,000 sets of averaged
693 randomly sampled genes (each set had the same number of genes as the number of markers),
694 divided by the standard deviation of the background signal. Enrichment scores for each nucleus
695 were transformed into a probability distribution by dividing by the sum of cell-type enrichment
696 scores. For each nucleus, we compared the top two most likely cell-types, retaining nuclei where
697 the top predicted cell-type had a two-fold greater probability than the next most likely assignment.
698 We used these high-confidence cells to train a regularized logistic multinominal classifier with the
699 R package, *glmnet*. Cell-type classifications with less than 10 nuclei in the training set were
700 excluded. We used a LASSO L1 penalty to regularize the logistic classifier, modeling the training
701 set of nuclei as observations and TMM gene accessibility scores as variables. We balanced
702 observations by weighting by the inverse frequency of cell-types in the training set. The model
703 was trained with 10-folds and evaluated by testing a 20% hold-out set of nuclei. The predicted
704 cell-type for each nucleus in the atlas was taken as the cell-type with the greatest probability if
705 the probability ratio between the best and next best assignment was greater than five-fold,
706 otherwise labeled as 'unknown'. Using these per-cell assignments, we defined subclusters as the
707 majority cell-type if greater than 50% of nuclei in the cluster were in agreement, labelling clusters
708 with two or more majority cell-types as 'mixed' and all other clusters as 'unknown'. All cell-type
709 labels from these three automated approaches were manually reviewed by careful evaluation with
710 UMAP gene accessibility score embeddings and cluster aggregated coverages for all marker
711 genes and refined *ad hoc*.
712
713 **STARR-seq analysis**
714 Single bp-resolution enhancer activities were available from a previous study[10]. Enhancer activity
715 (defined as the $\log_2$ ratio between RNA and DNA input fragments scaled per million) for each ACR
716 was taken as the maximum over the entire ACR. A control set of regions was generated to match

717 each ACR with the following criteria: (*i*) GC content within 5%, (*ii*) physically constrained to within
718 50-kb of an ACR, and (*iii*) the same length (500-bp) distribution. The same set of control regions
719 was used throughout the analysis.
720
721 **Analysis of differential chromatin accessibility**
722 Next, we implemented a logistic regression framework based on binarized ACR accessibility
723 scores for assessing the importance of each ACR to cluster membership by estimating the
724 likelihood ratio between logistic models with, and without a term for cluster membership.
725 Specifically, for each cluster, we compared binarized ACR accessibility scores to a reference
726 panel of uniformly sampled nuclei from each organ (111 nuclei from each organ) where the total
727 number of reference nuclei was set to the average number of nuclei per cluster (n=666). We then
728 fit two generalized linear logistic regression models (Eq. 10-11), with and without a term for
729 membership to the cluster of interest.
730
731 10. $logit(p_{ij}) = u_i + \alpha_j + \beta_j + \varepsilon_i$
732 11. $logit(p_{ij}) = u_i + \beta_j + \varepsilon_i$
733
734 Where p_{ij} is the probability that ACR i is accessible in nucleus j, u_i is the proportion of nuclei
735 where ACR i is accessible, α_j is the cluster membership of nucleus j, β_j is the $\log_{10}$ number of
736 accessible ACRs in nucleus j and ε_i is the error term for the ith ACR. We then used a likelihood
737 ratio test to compare the fits of the two models and estimated the false discovery rate (FDR) using
738 the Benjamini-Hochberg method to identify ACRs that were significantly differentially accessible
739 across clusters by conditioning on FDR < 5% and fold-change threshold greater than two. ACRs
740 meeting these criteria with positive Z-scores in nine or fewer clusters (< 10% of clusters) were

741 considered as cluster-specific. Analysis of differential gene accessibility was performed as
742 described in the section titled “Cell-type annotation”.
743
744 **GO gene set enrichment analysis**
745 Gene set enrichment using GO biological process terms was performed using the R package
746 *fgsea.* For each cluster, test statistics were multiplied by the sign of the $\log_2$ fold-change value
747 versus the reference panel. GO terms with gene sets less than 10 and greater than 600 were
748 excluded from the analysis. GO terms were considered significantly enriched at FDR < 0.05
749 following 10,000 permutations.
750
751 **Motif analysis**
752 Motif occurrences were identified genome-wide with *fimo* from the MEME suite toolset[58] using
753 position weight matrices (PWM) based on DAP-seq data in *A. thaliana* and *Zea mays*[59,60]. To
754 identity TF motifs associated with cell-type specific ACRs, we ranked the top 2,000 ACRs in each
755 cell-type by Z-scores derived from CPM normalized accessibility values (see section above
756 “Nuclei clustering”). As a reference for comparison, we identified 2,000 “constitutive” ACRs that
757 varied the least and were broadly accessible across clusters. The number of ACRs containing a
758 specific motif was compared to the frequency of constitutive ACRs harboring the same motif using
759 a binomial test for each cell-type and motif. To control for multiple testing, we used the Benjamini-
760 Hochberg method to estimate the FDR, considering tests with FDR < 0.05 as significantly different
761 between the focal cell-type and constitutively accessible regions. Maize homologs of *A. thaliana*
762 TFs were identified using protein fasta alignments from BLAST+ v2.10.0 with an E-value cut-off
763 of 1e-5. Only fasta sequences classified as transcription factors from either species were
764 considered during alignment. To narrow the list of putative orthologs based on functional similarity
765 to *A. thaliana* TFs, we filtered alignments with less than 30% identity, removed maize TFs
766 classified as belonging to a different family, and selected the homolog with the greatest Pearson

767 correlation coefficient (PCC) with respect to the motif deviation score. Motif deviation scores of
768 specific TF motifs among nuclei were estimated using *chromVAR*[61] with the non-redundant core
769 plant PWM database from JASPAR2018. The input matrix for *chromVar* was filtered to retain a
770 minimum of 50 accessible nuclei per ACR and barcodes with at least 50 accessible ACRs. We
771 visualized differences in global motif usage per nucleus by projecting deviation scores onto the
772 UMAP embeddings.
773
774 **Analysis of cell-type specific selection signatures**
775 Multi-locus allele-frequency differentiation signals between chronologically sampled elite maize
776 inbred lines were mapped onto ACRs[19], where the selection score for an ACR was taken as the
777 maximum XP-CLR value within the 500-bp ACR interval. To identity cell-types associated with
778 increased signatures of selection, the top 2,000 ACRs defined by standardized quantile-scaled
779 CPM chromatin accessibility (Z-scores, see above "Nuclei clustering") were identified for each
780 cell-type. The mean XP-CLR scores per-cell type were standardized by the mean and standard
781 deviation of randomly sampled ACRs (n=2,000) without replacement across 1,000 permutations,
782 where each permutation estimates the mean XP-CLR scores of a random subset of 2,000 ACRs
783 from the total list of 165,913 possible ACRs. Enrichment Z-scores were converted into *P*-values
784 using the R function *pnorm* (log.p=T, lower.tail=F) and used to estimate FDR via the Benjamini-
785 Hochberg method with the R function *p.adjust* (method="fdr").
786
787 **Analysis of co-accessible ACRs**
788 To enable comparison with previously identified Hi-C and HiChIP loops[10], we constrained the
789 distance between co-accessible ACRs to the same range as loops identified in leaf Hi-C and
790 HiChIP (minimum loop distance = 20-kb). Co-accessible ACRs and Hi-C/HiChIP loops were
791 considered overlapping if both anchors overlapped by at least 50-bp. We compared motif
792 composition of co-accessible ACRs by scoring motif occurrence as binary for each ACR and

793 estimating a Jaccard similarity score on the union of motif sets. Motif similarity scores for co-
794 accessible ACRs in each cell-type were compared to a null distribution by repeating Jaccard
795 similarity calculations for non-co-accessible ACR-ACR connections (constraining the null
796 connections to blocks of 1,000 ACR on the same chromosome with the same ACR-ACR distance
797 distribution as co-accessible ACRs) across 1,000 permutations. To identity motifs enriched at co-
798 accessible ACR anchors, we first estimated the proportion of co-accessible ACRs with an identical
799 motif at both anchors for each motif and cell-type. Then, we constructed the same number of
800 random ACR-ACR connections as co-accessible ACRs, again estimating the proportion of links
801 with an identical motif at both anchors, building a null distribution over 1,000 random
802 permutations. The estimated proportion of co-accessible ACRs with identical motifs at both
803 anchors for each motif was transformed to a Z-score by subtracting and scaling by the mean and
804 standard deviation of the null distribution. Z-scores were converted to *P*-values using the R
805 function, *qnorm* with non-default parameters (log.p=T, lower.tail=F). FDR values were estimated
806 using *p.adjust* (method="fdr"). Co-accessible motif scores were plotted as heatmaps using
807 *heatmap.2* by subtracting and dividing observed with expected proportions. Rows and columns
808 were clustered with *hclust* (method="ward.D2").
809
810 **Pseudotime analysis**
811 Pseudotime trajectories were constructed similar to previous methods[62]. Briefly, nuclei were
812 ordered based on the principal component space by fitting a continuous trajectory via a smooth
813 spline on the Euclidean distances of each nuclei to a predefined order of cell-types. For feature
814 analysis (ACRs, motifs, and TF activity) across pseudotime, nuclei were sorted by ascending
815 pseudotime. The ACR x nucleus matrix was filtered to retain differentially accessible ACRs (see
816 section "Analysis of differential accessibility across pseudotime" below) with at least one nucleus
817 defined as accessible. For each ACR, we fit a generalized additive model with the binary
818 accessibility scores as the response and a smoothed pseudotime component as the dependent

819 variable [s(pseudotime, bs="cs")] with a binomial error term and a logit-link function with *gam* from
820 the *mgcv* R package. Predicted accessibility scores across pseudotime were generated from 500
821 equally spaced interpolated points covering the range of pseudotime values. Finally, predicted
822 accessibility scores were mean-centered, standardized and constrained to the range ± 1 for each
823 ACR. Model specification for motif deviations and TF gene accessibility analysis was similar to
824 ACR pseudotime analysis with the exception of a Gaussian error distribution, and TF gene
825 accessibility was normalized by the row maximum rather than rescaling on a ± 1 distribution.
826

827 **Analysis of differential accessibility across pseudotime**

828 To identity differentially accessible ACRs across pseudotime, we fit normalized accessibility
829 residuals (Pearson residuals from a generalized linear logistic regression model with $\log_{10}$ number
830 of accessible ACRs per barcode as the dependent variable, see section "Nuclei Clustering"
831 above) as the response and pseudotime as the dependent variable using a natural spline with six
832 degrees of freedom [ns(pseudotime, df=6)] from the R package *splines* for each trajectory. We
833 took an F-test based approach for hypothesis testing of differential accessibility across
834 pseudotime by comparing the variance explained by the splined linear model with that of the
835 residuals normalized by degrees of freedom. *P*-values from the model were used to estimate
836 Benjamini-Hochberg FDR values with the R function *p.adjust* (method="fdr"), where a FDR
837 threshold < 0.05 denoted statistical significance for differentially accessible ACRs across
838 pseudotime. To identify genes and TF motifs with differential accessibility across pseudotime, we
839 fit the linear splined regression model with the normalized gene accessibility scores and motif
840 deviations from each nucleus, respectively, similar to the analysis of ACRs.
841

842 **Aligning pseudotime trajectories between *A. thaliana* and *Z. mays***

843 To enable comparison of companion cell development between *A. thaliana* and *Z. mays*, we first
844 identified putative one-to-one orthologs using *OrthoFinder* (v2)[63]. Gene accessibility scores for
845 10,976 putative orthologs were imputed using a diffusion-based approach[56,64] and scaled from 0
846 to 1 across pseudotime for barcodes associated with companion cell development in *A. thaliana*
847 and *Z. mays*. To account for different distributions, pseudotime coverage, and number of
848 barcodes between species, we used the R package, *cellAlign,* that interpolates, scales, and
849 weights gene accessibility scores on a fixed set of (n=200) equally spaced points (width
850 parameter: winSz=0.1) from two trajectories to remove technical biases inherent to each data
851 set[65]. For each putative ortholog, we performed global alignment of gene accessibility scores
852 across *A. thaliana* and *Z. mays* pseudotime using the dynamic time warping algorithm with default
853 settings in *cellAlign.* We then extracted the pseudotime shifts, representing the extent of gene
854 accessibility deviation at any given point along the trajectory, for each putative ortholog. We
855 clustered genes into two groups based on pseudotime shifts across companion cell development
856 using k-means clustering. To identify conserved gene accessibility patterns across pseudotime,
857 we clustered the normalized distances between *A. thaliana* and *Z. mays* putative orthologs using
858 a mixture model (G=2) with the R package, *mclust.* The mixture model identified a bimodal
859 distribution of normalized distances with 0.15 as a natural cut-off for defining conserved
860 accessibility patterns. Putative orthologs with normalized distances less than the cut-off were
861 placed in a third group defined as conserved. The above analysis was repeated with TF motif
862 deviations scores for 440 TF motifs, without the need for ortholog searching as the same TF
863 position weight matrices were used for both species, affording identical TF motif labels.
864

865 **DATA AVAILABILITY**

866 Supplementary Data are available on the online versions of this manuscript. Raw and processed
867 data has been deposited in NCBI GEO database under accession code GSEXXXXXX. Cell-type

resolved data can be viewed through our public Plant Epigenome JBrowse Genome Browser[66] (URL available upon publication).

CODE AVAILABILITY

Code used throughout the analysis will be made available upon publication.

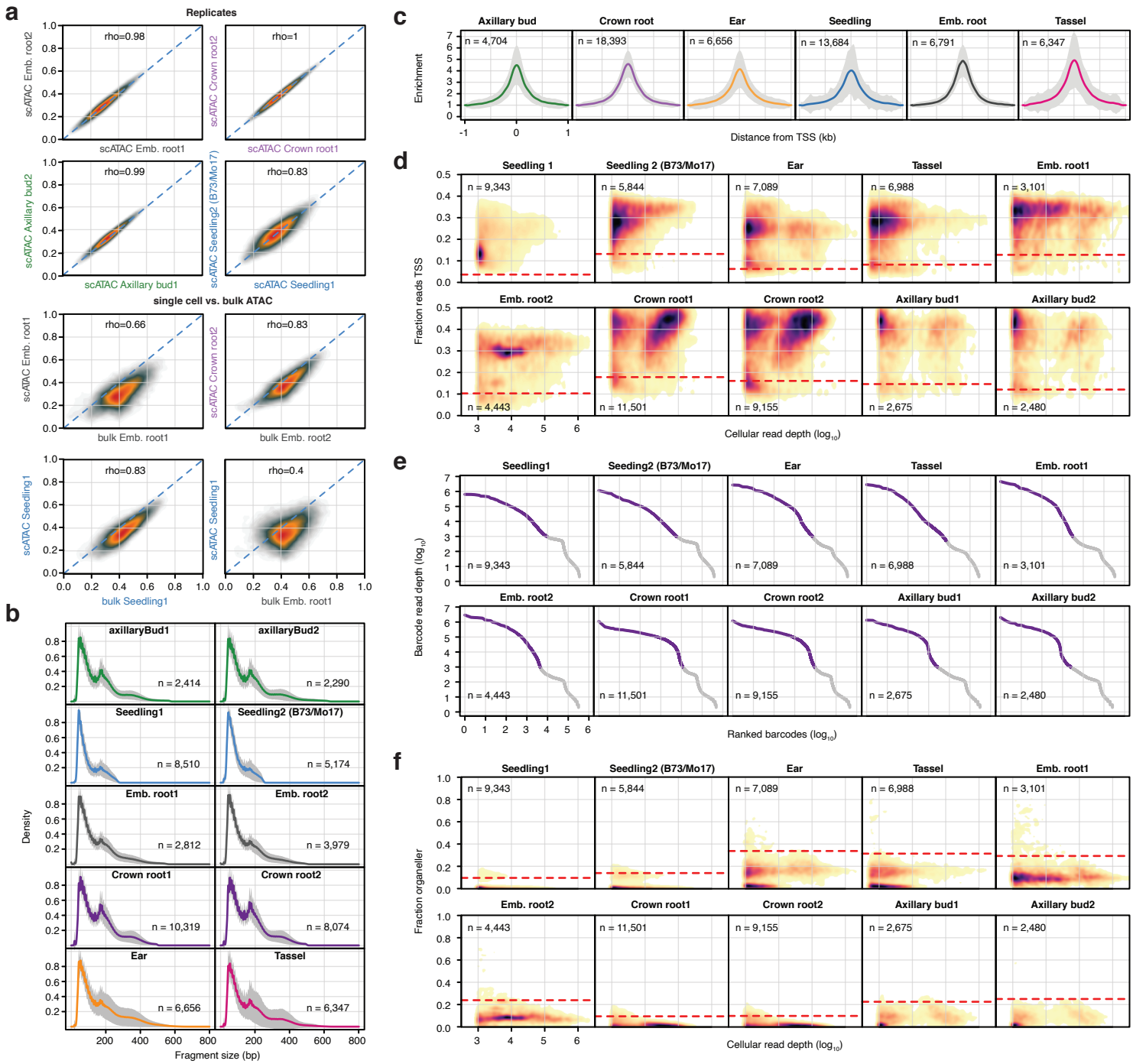

Extended Data Fig. 2: Cell calling and barcode quality control

a, Comparison of normalized (0-1) read depths at the union of all peaks across bulk and single-cell samples (n=265,992) between replicated libraries, and between bulk and single-cell ATAC-seq assays. **b**, Fragment length distributions for each library. Solid lines indicate the average distribution across cells within the sample. Grey polygons represent the standard deviation across cells in the library. **c**, Enrichment plots centered on 2-kb windows surrounding TSSs for barcodes in each tissue. Grey polygons indicate the standard deviation across cells within the noted tissue. **d**, Density scatter plots of log10 transformed barcode read depths (x-axis) by the fraction of Tn5 integration sites mapping to within 2-kb of transcription start sites (TSSs). Dashed red lines indicate the threshold of two standard deviations from the mean used to filter lower quality barcodes. **e**, Knee plots illustrating log10 transformed cellular read depths of log10 ranked barcodes across libraries. **f**, Density scatter plots of log10 transformed barcode read depths (x-axis) by the fraction of Tn5 integration sites derived from organeller sequences (chloroplast and mitocondrial) relative to the total number of unique Tn5 integration sites associated with cognate barcode. Dashed red lines indicate the threshold of two standard deviations from the mean used to filter lower quality barcodes.

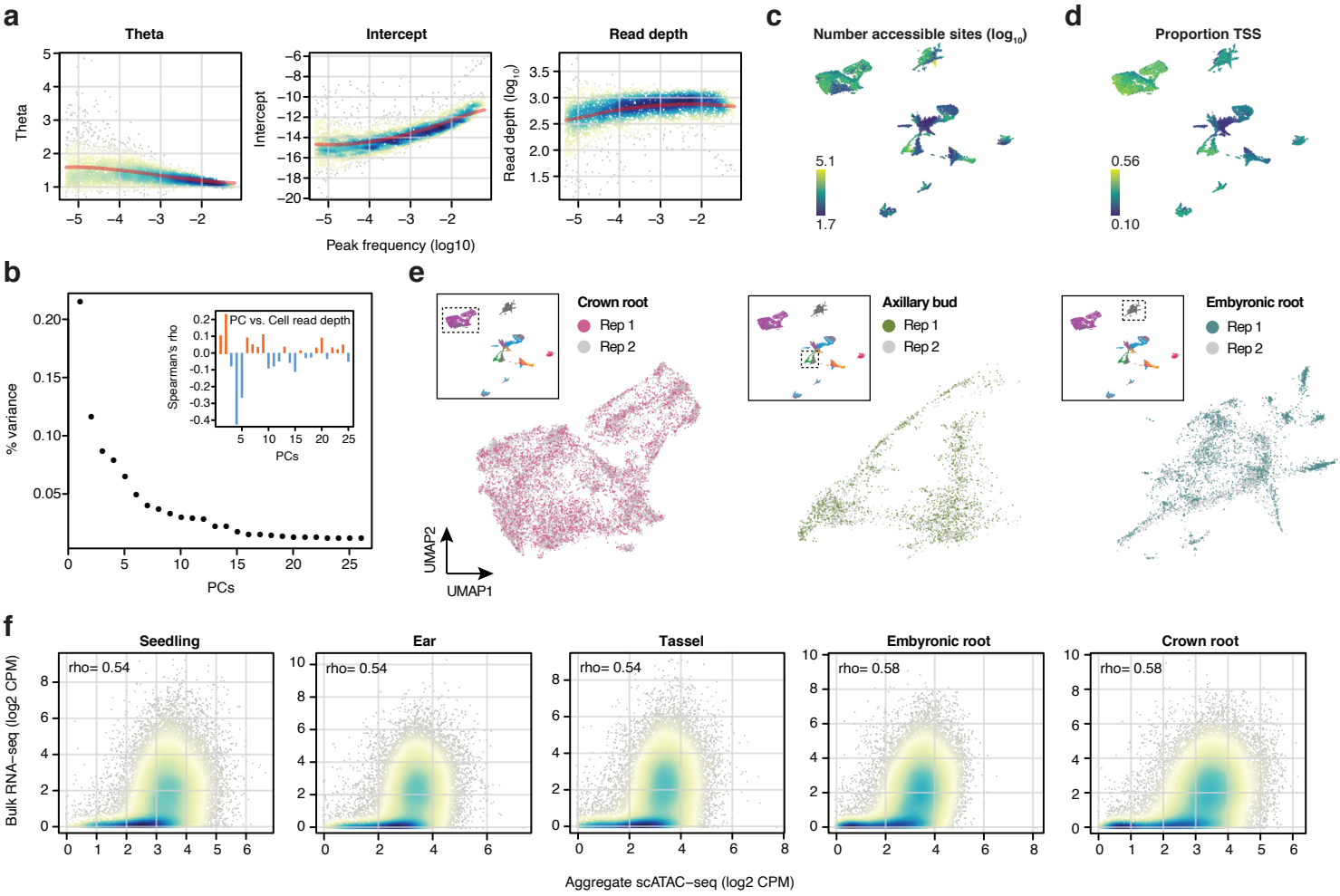

Extended Data Fig. 3: Clustering metrics and comparison of bulk gene accessibility and expression
a, Parameter regularization of model coefficients (y-axes) with respect to ACR usage (x-axes; proportion of nuclei with at least one Tn5 integration site in an ACR). **b**, Proportion of variance captured by the first 26 PCs. Inset: Spearman's correlation of principal components with cell read depth (log10-transformed). **c**, Number of accessible sites per cell (log10). **d**, Proportion of Tn5 integrations within 2kb of gene TSSs per cell. **e**, Co-localization of nuclei barcodes from different biological replicates for three organs. **f**, Comparison of bulk RNA-seq expression levels (y-axis, log2 CPM) versus aggregate scATAC-seq gene accessibility scores (x-axis, log2 CPM) within an organ.

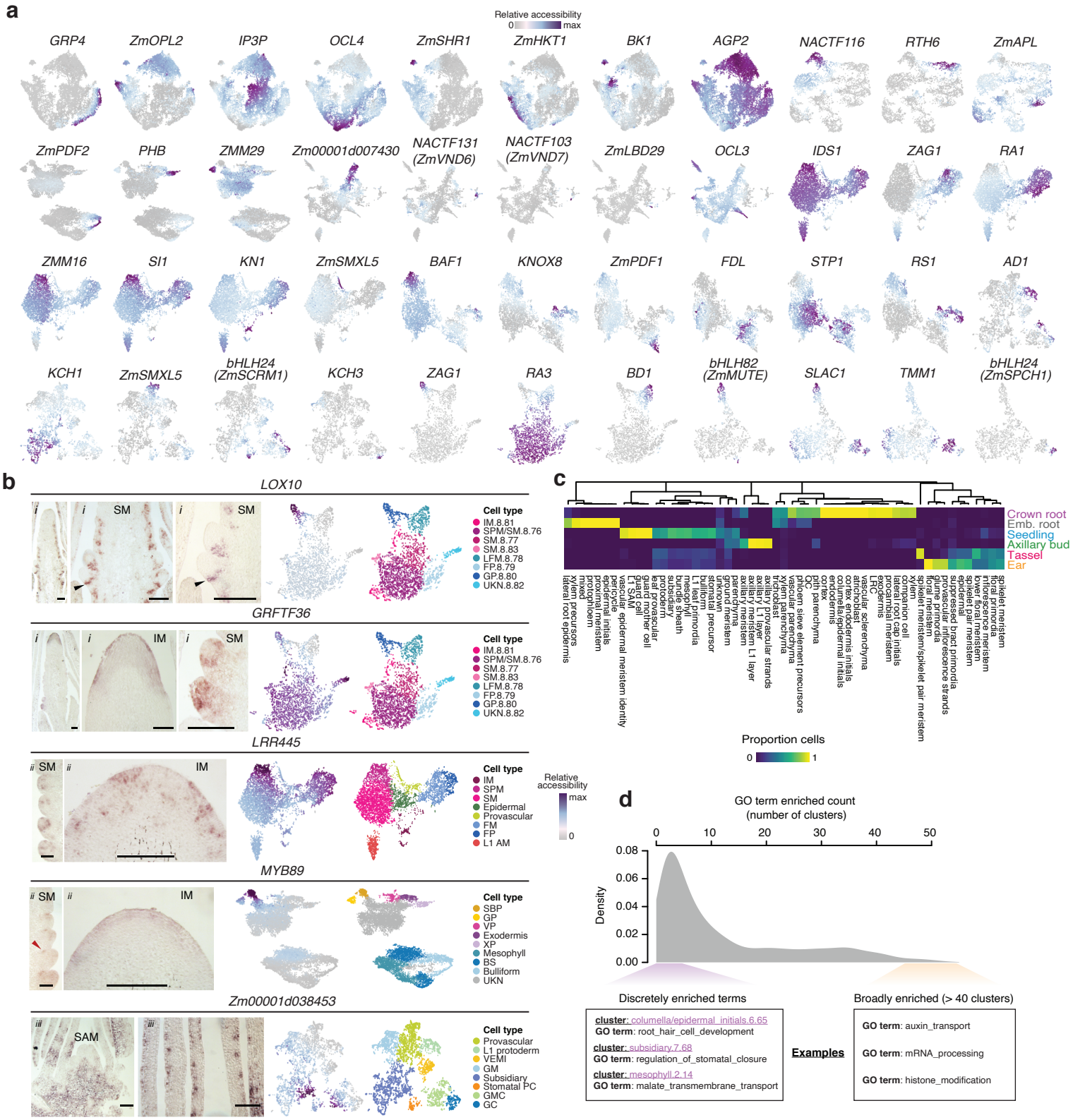

Extended Data Fig. 4: Cell-type annotation and GO enrichment

a, UMAP embeddings of nuclei barcodes colored by low (grey) to high (dark purple) gene activity values of cell-type specific marker genes. **b**, RNA *in situ* hybridization showing expression of *LOX10* in glume primordia and *GRFTF36* in IM and SMs of staminate inflorescence; *LRR445* in the IM periphery and SPMs and *MYB89* in the IM and suppressed bract primordia of pistillate inflorescence; Zm00001d038453 in ground tissue of SAM and leaf primordia sections. Gene accessibility scores and predicted cell-types are shown on the right. *i*, tassel primordia. *ii,* ear primordia. *iii*, SAM/leaf. Black triangles point to the glume primordia. Red triangles point to suppressed bract primordia. Size bars illustrate 100-um. AM, axillary meristem; BS, bundle sheath; GC, guard cell; GM, ground meristem; GMC, guard mother cell; GP, glume primordia; IM, inflorescence meristem; L1, layer 1; LFM, lower floral meristem; SAM, shoot apical meristem; SBP, suppressed bract primordia; SM, spikelet meristem; SPM; spikelet pair meristem; Stomatal PC, stomatal precursor; UKN, unknown; VEMI, vascular/epidermal meristematic identity; VP, vascular parenchyma; XP, xylem parenchyma. **c,** Proportion of cells within subcluster (column) derived from one of six organs (rows). **d,** Distribution of GO term enrichment across clusters, where the x-axis indicates the number of clusters in which a GO term is significantly enriched.

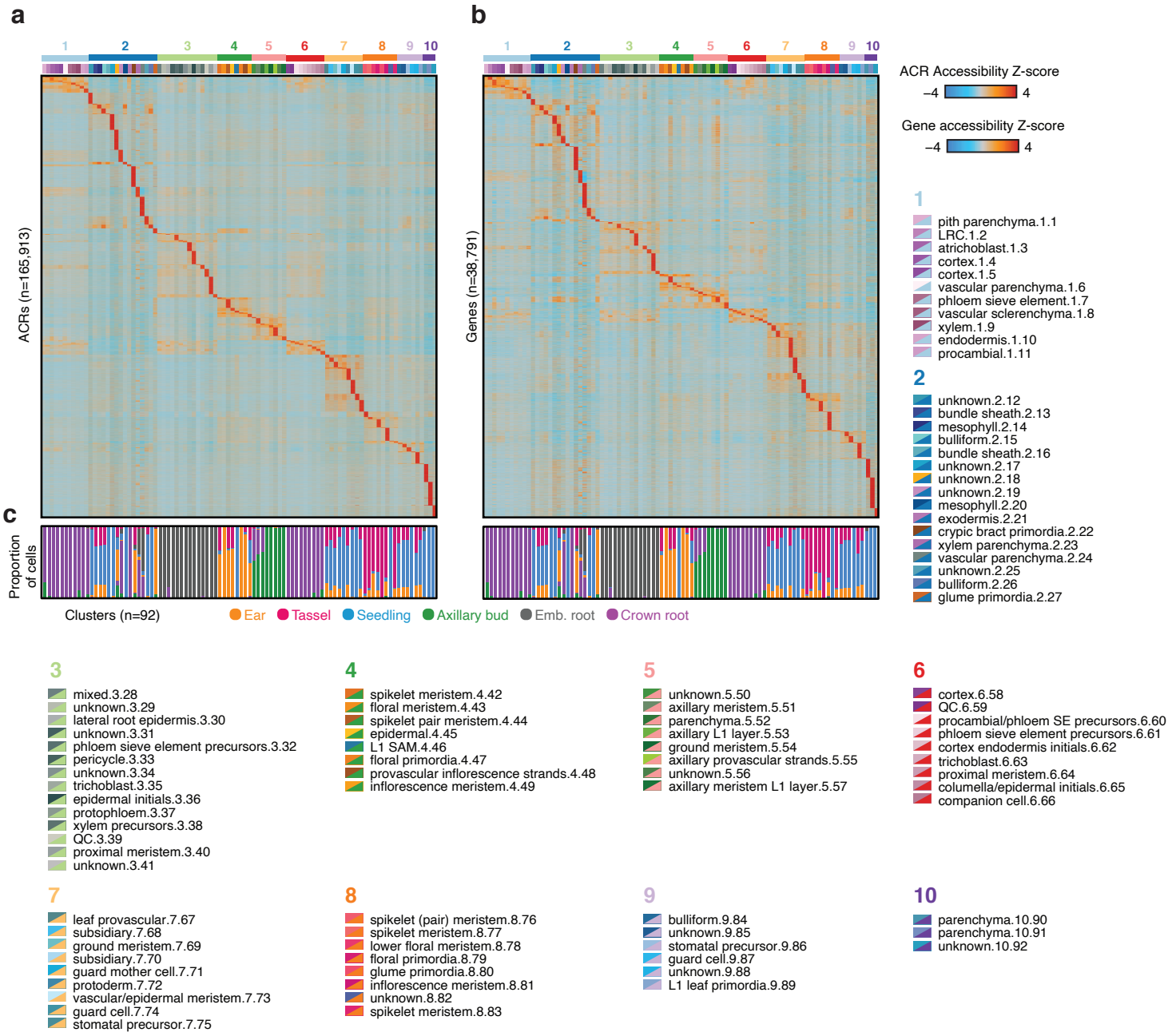

Extended Data Fig. 5: Chromatin accessibility variation across plant cell-types

a, Row chromatin accessibility Z-scores across cell-types. Cell-type and subcluster labels are located adjacent to the heatmap in identical order as the matrix. The first number after the cell-type label indicates the major cluster number, while the second number represents the subcluster ID. Legend colors: top left triangle, subcluster (corresponds to the sub-cluster annotation on heatmap). bottom right triangle, major cluster (corresponds to the major cluster annotation on heatmap). **b**, Row gene accessibility Z-scores across cell-types. **c**, Proportion of cells derived from one of six organs within each cell-type/subcluster.

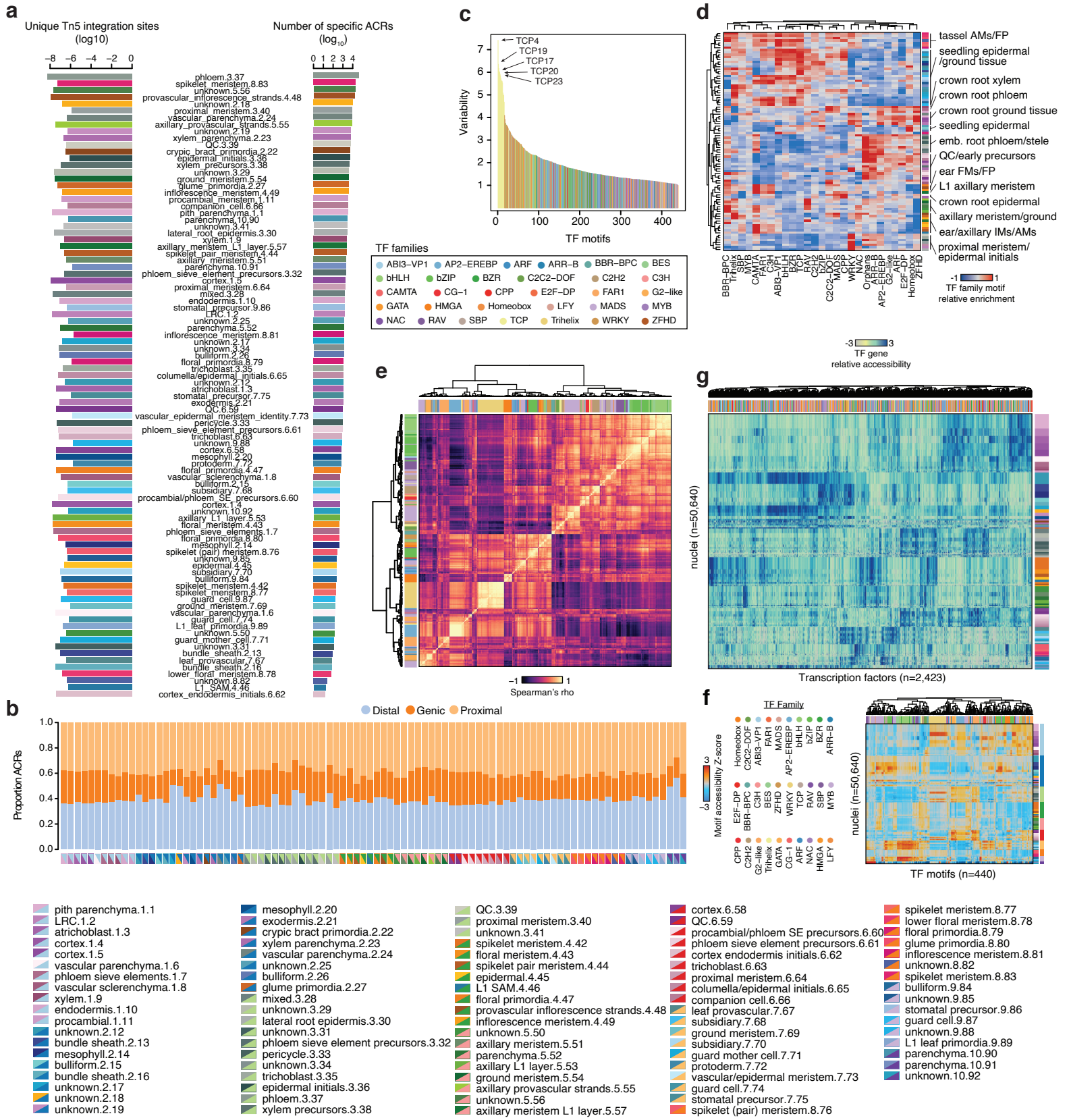

Extended Data Fig. 6: Transcription factor motif variation underly dynamic accessible regions

a, Comparison of cell-type specific ACR counts (by cell-type) and the number of unique Tn5 integration sites. **b,** Proportion of distal, genic and proximal ACRs per cell-type. **c,** Ranked TF motif variability across cells, colored by TF family. **d,** Mean TF family motif enrichment (average deviation scores per cell-type per TF family) across cell-types scaled to +/- 1. **e,** Spearman's correlation coefficient (rho) between TF motifs (comparison of motif deviations across all nuclei). Row and column colors represent TF motif families. **f,** TF motif deviations for 440 TF motifs (columns) per nucleus (rows). The TF family for each corresponding motif is denoted by column header colors. Cluster identification (sub-cluster/major cluster) are illustrated as row header colors on the right side of the heatmap. **g,** Relative gene accessibility scores for 2,423 maize transcription factors (columns) for 50,640 nuclei (rows). Nuclei are sorted by sub-cluster cell-type (row color labels). A cell-type annotation color legend applicable to panels b, f, and g where left triangle reflects sub-cluster, right triangle indicates the major cluster.

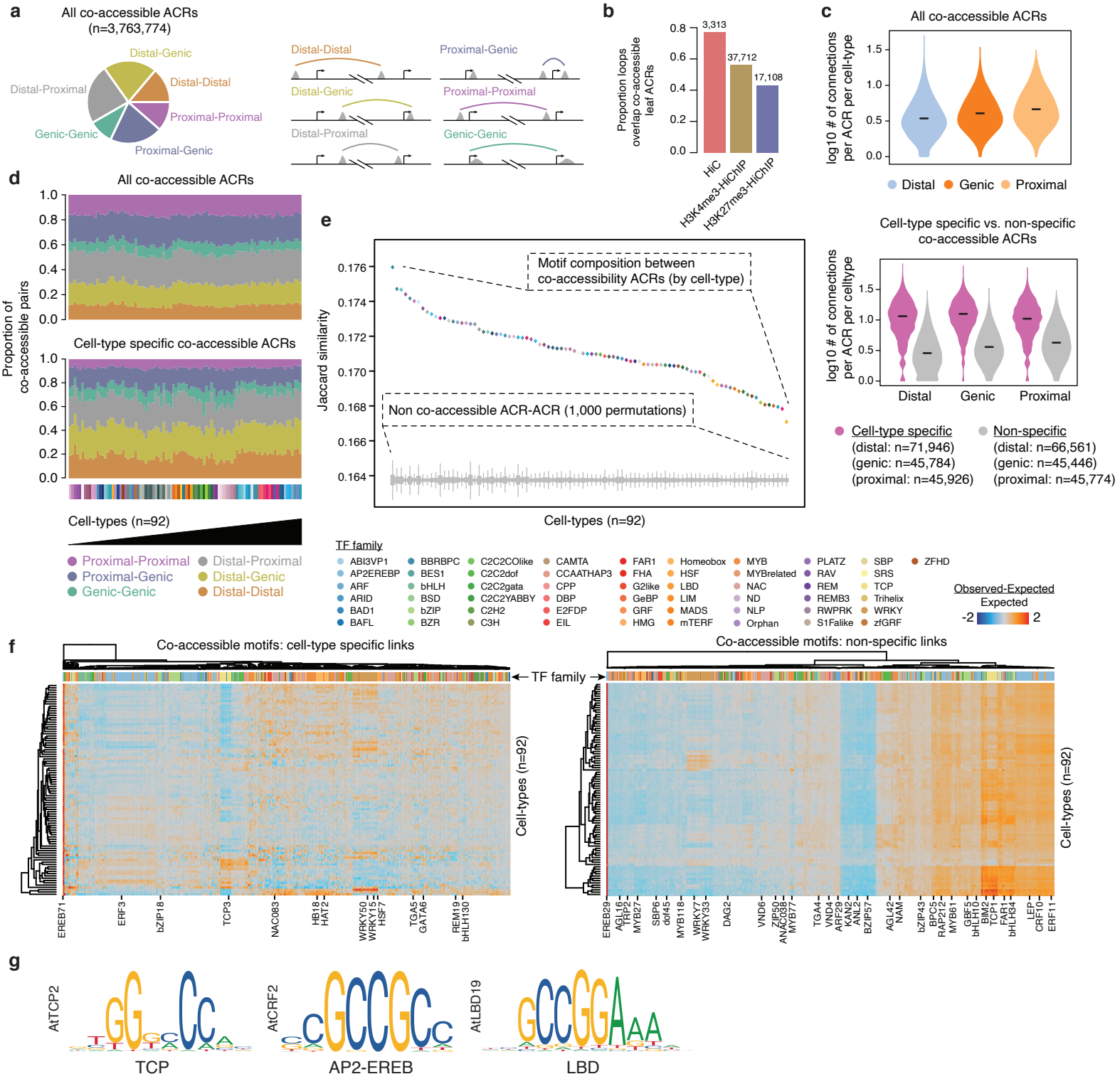

Extended Data Fig. 7: Co-accessible ACRs reflect in vivo chromatin interactions driven by coordinated TF activity
a, Proportions of co-accessible ACR types, illustrated by toy examples. **b**, Proportion leaf Hi-C, H3K4me3-HiChIP and H3K27me3-HiChIP chromatin loops that overlap co-accessible ACRs from leaf cell-types (clusters with greater than 50% of cell derived from seedlings). **c**, Top, log10 number of connections per ACR per cell-type from all co-accessible ACRs split by genomic context: distal, proximal, and genic. Bottom, log10 number of connections per ACR per cell-type from cell-type specific (purple) and non-specific (grey) co-accessible ACRs, split by genomic context. **d**, Proportion of co-accessible classifications by cell-type for all co-accessible ACRs (top) and cell-type specific co-accessible ACRs (bottom). **e**, Jaccard similarity of motif composition between co-accessible ACR edges by cell-type (colored diamonds) relative to the same number of random ACR-ACR links, permuted 1,000 times for each cell-type (grey boxplots). Box plots represent the interquartile range, grey lines indicate the permuted range. **f**, Heatmaps of observed proportion of co-accessible ACRs with the same motif embedded within link edges subtracted and divided by the expected proportion estimated by 1,000 permutations using random ACR-ACR links with the same number of co-accessible ACRs. **g,** Exemplary motifs enriched in reciprocal co-accessible ACRs for *TCP*, *AP2-EREB*, and *LBD* TF families.

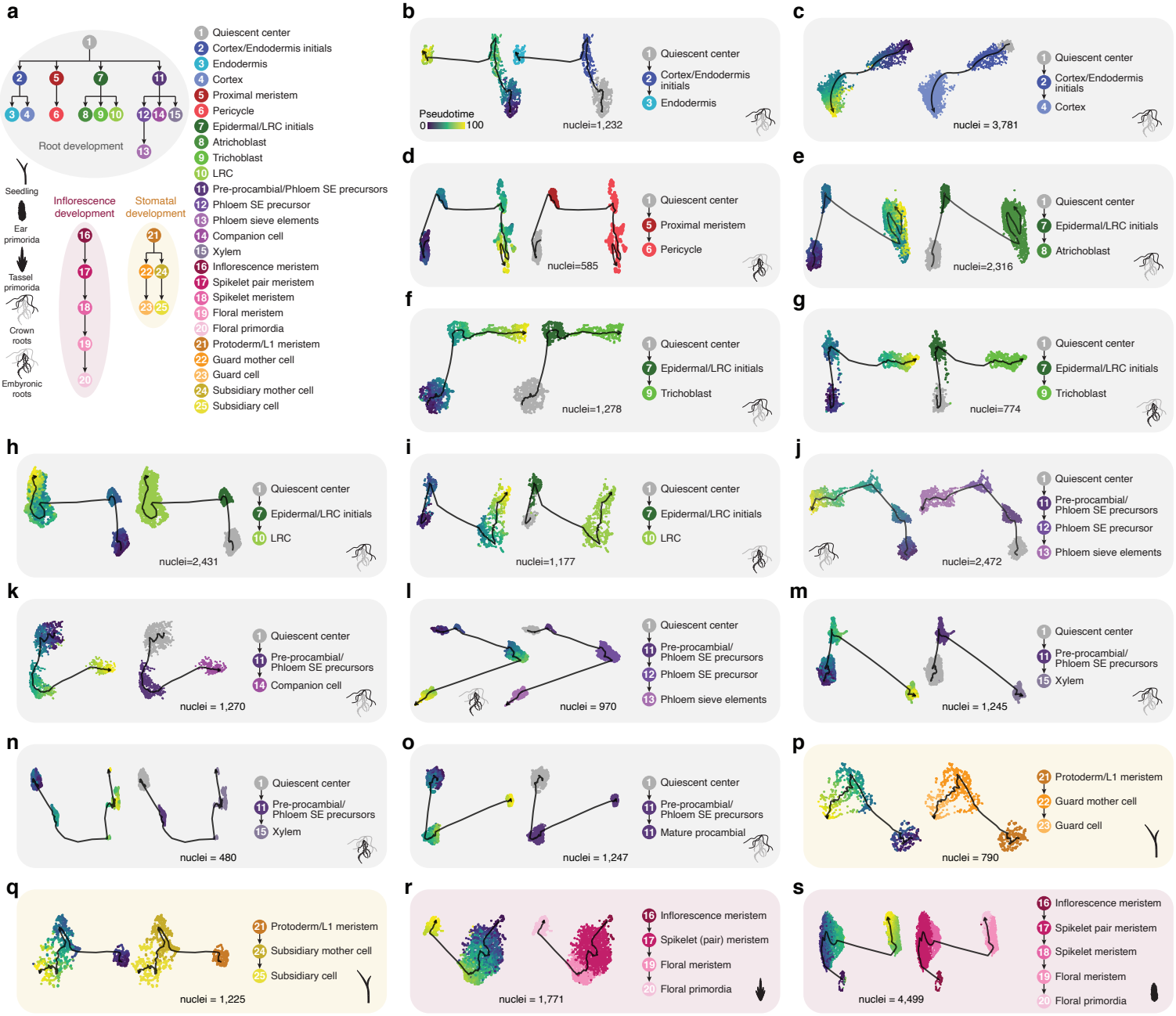

Extended Data Fig. 8: Pseudotime trajectory construction

a, Overview of pseudotime developmental trajectory analysis from four organs: root, seedling, tassel (staminate inflorescence), and ear (pistilate inflorescence). **b,** Endodermis development in crown roots. **c,** Cortex development in crown roots. **d,** Pericycle development in embryonic roots. **e,** Atrichoblast development in crown roots. **f,** Trichoblast development in crown roots. **g,** Trichoblast development in embryonic roots. **h,** Lateral root cap (LRC) development in crown roots. **i,** Lateral root cap (LRC) development in embryonic roots. **j,** Phloem sieve element (SE) development in crown roots. **k,** Companion cell development in crown roots. **l,** Phloem sieve element (SE) development in embryonic roots. **m,** Xylem development in crown roots. **n,** Xylem development in embryonic roots. **o,** Procambial development in crown roots. **p,** Guard cell development in seedling. **q,** Subsidiary cell development in seedlings. **r,** Floral primordia development in staminate inflorescence (tassel). **s,** Floral primordia development in pistilate inflorescence (ear).

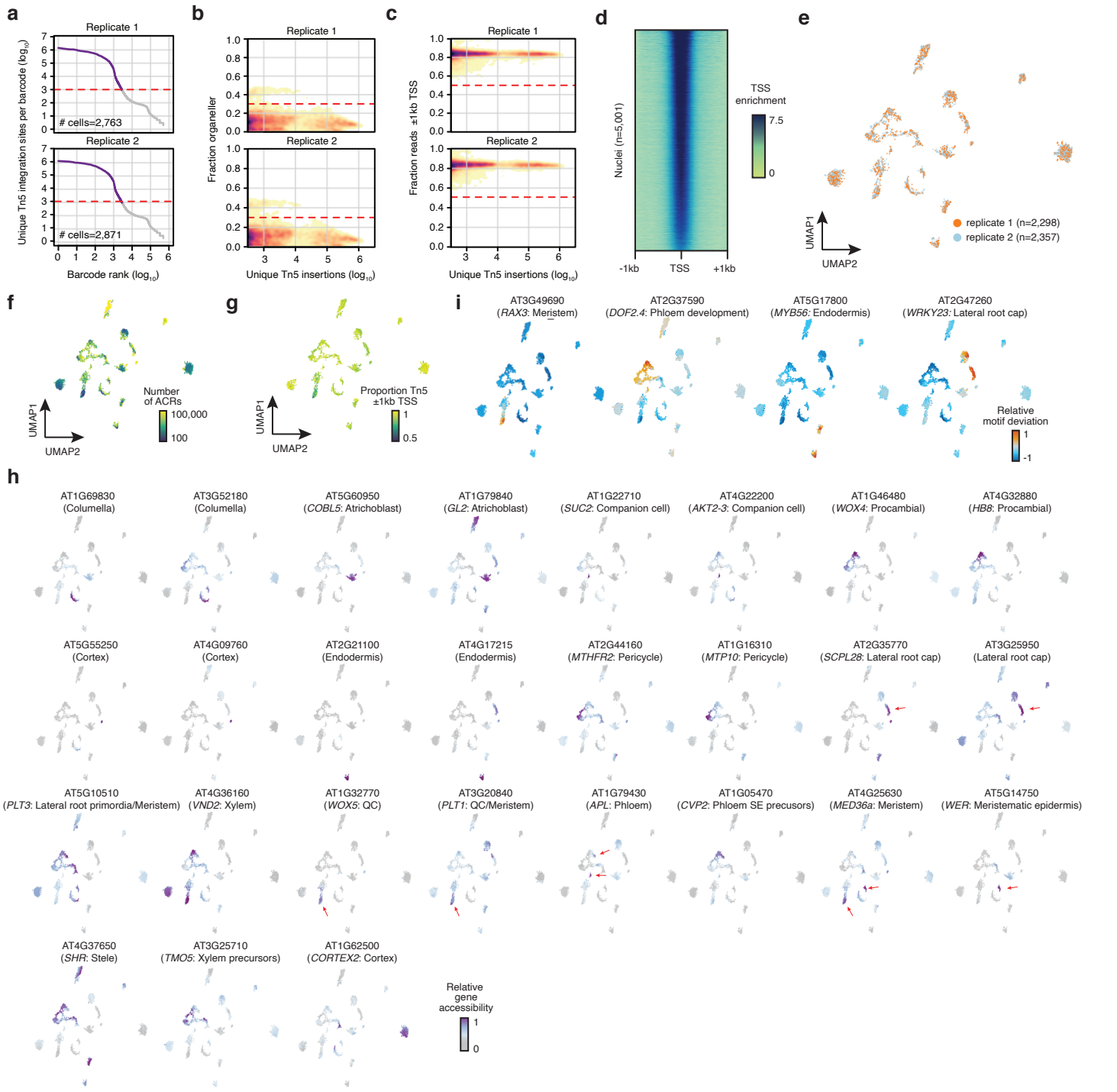

Extended Data Fig. 9: *Arabidopsis thaliana* root cell-type atlas

a, Knee plots for Arabidopsis thaliana root samples illustrating log10 transformed cellular read depths of log10 ranked barcodes across two biological replicates. **b,** Density scatter plots of log10 transformed barcode read depths (x-axis) by the fraction of Tn5 integration sites derived from organellar sequences (chloroplast and mitochondrial) relative to the total number of unique Tn5 integration sites associated with each barcode from the two biological replicates. Dashed red lines indicate the threshold of two standard deviations from the mean used to filter lower quality barcodes. **c,** Density scatter plots of log10 transformed barcode read depths (x-axis) by the fraction of Tn5 integration sites mapping to within 2-kb of transcription start sites (TSSs). Dashed red lines indicate the threshold of two standard deviations from the mean used to filter lower quality barcodes. **d,** Average TSS enrichment (normalized read depth adjusted by the two 10 bp windows 1-kb away from TSSs) across 5,001 Arabidopsis thaliana root barcodes (rows). **e,** UMAP (Uniform manifold approximation projection) embeddings of Arabidopsis thaliana root barcodes colored by biological replicate; **f,** total number of accessible chromatin regions (ACRs); **g,** the proportion of Tn5 integration sites within 1-kb of TSSs. **h,** Relative gene accessibility for 27 known cell-type/domain restricted marker genes used to inform cell-type annotation of Arabidopsis thaliana root clusters. **i,** Relative motif deviations for transcription factors with known cell-type specificities.

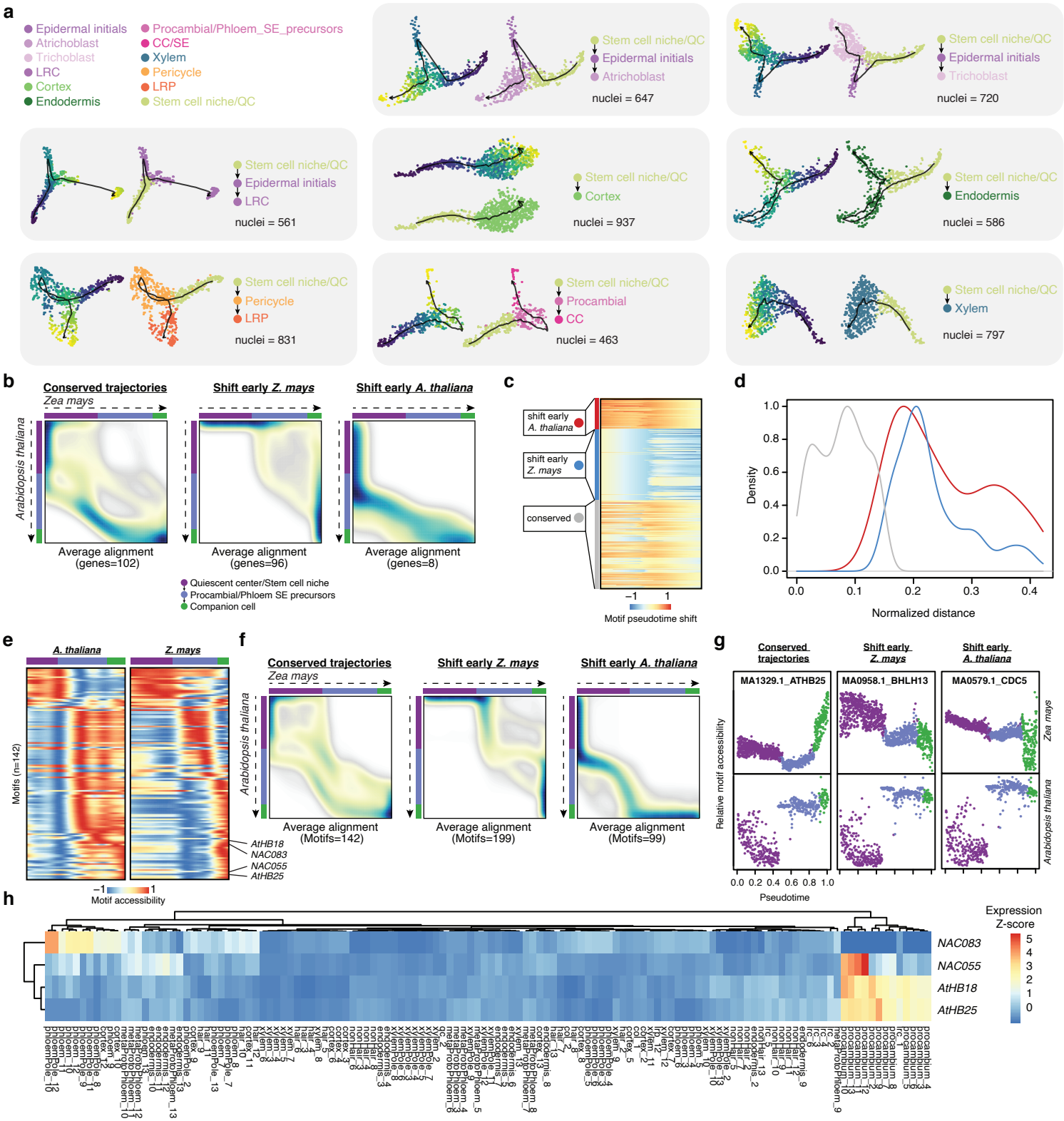

Extended Data Fig. 10: Dynamic and conserved chromatin accessibility across pseudotime between *Arabidopsis thaliana* and *Zea mays*

a, Pseudotime trajectories for Atrichoblast, Trichoblast, Lateral root cap (LRC), Cortex, Endodermis, Lateral root primordia (LRP), Companion cells (CC), and Xylem development. **b,** Averaged alignments of conserved, shift early *Z. mays*, and shift early *A. thaliana* putative orthologs. **c,** Pseudotime shifts of TF motifs between *A. thaliana* and *Z. mays*, clustered into k-means and conserved groups. **d,** Distributions of motif-motif normalized distances between *Z. mays* and *A. thaliana* for the three groups. **e,** Conserved motifs (n=142) ordered by pseudotime. Heatmaps for *A. thaliana* and *Z. mays* have identical row orders. **f,** Averaged alignments of conserved, shift early *Z. mays*, and shift early *A. thaliana* groups based on motif-motif global alignments from the dynamic time-warping algorithm. **g,** Examples of conserved, shift early *Z. mays*, and shift early *A. thaliana* motifs from both species. **h,** Gene expression Z-scores across *A. thaliana* FAC sorted root cell-types for the TFs recognizing the top four conserved motifs.

894 **FIGURE LEGENDS**

895 **Figure 1: Atlas-scale profiling of single nuclei chromatin accessibility in *Zea mays***

896 **a,** Overview of experimental protocol. Homogenized samples release nuclei that are extracted by
897 flow cytometry. Accessible chromatin is tagged by Tn5 and individual nuclei are distinctly
898 barcoded in disparate droplets following microfluidic separation, allowing droplet pooling and
899 library amplification prior to sequencing. **b,** Nuclei similarity clustering as a UMAP embedding
900 derived from the denoised quasibinomial residuals across all ACRs for each nucleus. UMAP
901 embedding of nuclei colored by **b,** organ identity and **c,** major cluster identity. **d,** UMAP
902 embedding of sub-cluster assignments following a second round of clustering within each major
903 cluster. **e,** Cell-type specific enrichment of gene accessibility for a subset of marker genes
904 associated with six different cell-types. **f,** Sub-cluster specific chromatin accessibility profiles
905 surrounding known marker genes for floral primordia, xylem precursors, and L1 epidermal cells.
906 Bold, circled numbers indicate the cognate major cluster shown in panel **c**. Sub-cluster numeric
907 identifications are present on the sides of the coverage plots. **g,** Top, gene accessibility for
908 *ZmGRFTF36*, an inflorescence and spikelet meristem enriched TF with no previously known cell-
909 type specificity. Bottom, RNA in situ hybridization of *ZmGRFTF36* in maize B73 staminate (tassel)
910 primordia. FP, floral primordia; IM, inflorescence meristem; LFM, lower floral meristem; SM,
911 spikelet meristem; SPM, spikelet pair meristem; TF, transcription factor; UKN, unknown.

912

913 **Figure 2: Characterization of accessible chromatin regions**

914 **a,** Distribution of enhancer activity (maximum $\log_2$[RNA/input]) for control regions (n=165,913),
915 constitutively accessible (n=113,393) and cluster-specific ACRs (n=52,520). The dash red line
916 indicates the overall mean. Orange lines reflect differences between the group mean and overall
917 mean. **b,** Distribution of ACR distances to the nearest gene. Inset, distribution of ACR genomic
918 context. **c,** Relative DNA methylation levels 2-kb flanking ACRs. **d,** Relative enrichment of

919 polymorphisms after normalizing by mapability for 5-kb regions flanking cell-type specific and
920 constitutive ACR summits. Smoothed splines are shown as dark lines. **e,** Relative enrichment of
921 significant GWAS polymorphisms relative to all polymorphisms for 5-kb regions flanking cell-type
922 specific and constitutive ACR summits. **f,** Enrichment of signatures of selection (XP-CLR) in the
923 top 2,000 ACRs for all cell-type clusters. The 20 most enriched cell-types are highlighted on the
924 left. AM, axillary meristem; CC, companion cell; FM, floral meristem; FP, floral primordia; IM,
925 inflorescence meristem; QC, quiescent center; SM, spikelet meristem; SPM, spikelet pair
926 meristem. **g,** Average motif coverage for ACRs (n=165,913) and control regions (n=165,913).
927 Shaded polygon, 95% confidence intervals. **h,** Enrichment of TF motifs in the top 2,000 ACRs
928 ranked by Z-score for each cell-type compared to the top 2,000 most constitutive ACRs via
929 binomial tests. FDR was estimated by the Benjamini-Hochberg method. **i,** Comparative heatmaps
930 for matched TF gene accessibility (bottom) and motif deviation (top) Z-scores across clusters. **j,**
931 Gene accessibility scores for five maize transcription factors (top) and their associated motif
932 deviations (bottom).
933
934 **Figure 3: Co-accessible ACRs reflect *in vivo* chromatin interactions and are established**
935 **by cell-type specific TFs. a**, Comparison of ear and seedling co-accessible ACRs across nine
936 cell-types at the genetically mapped *tb1-enhancer* domestication locus (highlighted region). Link
937 height reflects co-accessibility scores between ACRs across cells in a cluster. **b**, Average
938 normalized Hi-C signal across 4-kb windows centered on ACRs equally distributed into three
939 groups (each group: n=54,904) based on the number and strength of participating co-accessible
940 links. **c**, Co-accessible ACR interaction frequency across clusters. Inset: Single cell-type co-
941 accessible links (n=1,018,417) for different genomic contexts. **d**, Standardized (row-wise) number
942 of connections for each ACR (rows) by cell-type (columns). Column color map reflect cell-types
943 from the legend in Extended Data Fig. 4. Gene-proximal ACRs for a subset of marker genes are

944 indicated on the right. **e**, Right, chromatin accessibility and co-accessible ACR links surrounding
945 the *UB2* locus associated with ear row number and tassel branch number quantitative traits. Black
946 arrow indicates a distal ACR upstream of *UB2* present only in spikelet meristems. Co-accessible
947 links with an edge within 2-kb of *UB2* are colored pink while remaining links are grey. Link height
948 represents co-accessibility strength. Left, close-up of accessibility profiles of *UB2*. **f**, Distributions
949 of average ACR-ACR links across cell-types for ACRs that overlap (purple) and do not overlap
950 (grey) phenotype-associated genetic variants from maize GWAS. The median of each distribution
951 is shown as a white horizontal line. Violin plots present the entire range of average number of
952 connections on a log scale. Hypothesis testing was conducted within the *R* statistical framework
953 via Wilcoxon rank sum test. **g,** Distributions of average ACR-ACR links cell-types for ACRs with
954 (blue) and without (grey) enhancer activity ($\log_2$ RNA/input greater than 0). Hypothesis testing
955 and distribution illustration was performed similarly as panel **f**.
956
957 **Figure 4: Chromatin accessibility is dynamic across pseudotime and conserved between**
958 ***Arabidopsis thaliana* and *Zea mays***
959 **a,** Overview of pseudotime trajectory analysis. Inflorescence development includes trajectory
960 construction of pistillate and staminate inflorescence, and root development encompasses
961 embryonic and crown root trajectories. **b,** UMAP embedding of companion cell developmental
962 trajectory depicting cell-types (left) and pseudotime progression (right). **c,** Relative motif
963 deviations for 440 TF motifs (left, rows), 402 TF gene accessibility scores (middle, rows), and
964 relative accessibility of 8,094 ACRs (right, rows) associated with pseudotime (columns). Four
965 motifs enriched along the trajectory gradient are shown on the left. ACRs, accessible chromatin
966 regions; TF, transcription factor. **d,** Genome browser screenshots of cell-type specific chromatin
967 accessibility profiles along the developmental trajectory for quiescent center, procambial/phloem
968 sieve element precursor, and companion cell at associated marker gene loci. **e,** UMAP
969 embedding based on whole-genome chromatin accessibility profiles of 4,655 *A. thaliana* root

970 nuclei. **f,** UMAP embedding of companion cell developmental trajectories in *A. thaliana* depicting
971 cell-types (left) and pseudotime progression (right). Motifs, TFs, and ACRs with significant
972 association with pseudotime are shown as heatmaps below. **g,** Per-gene pseudotime shift scores
973 from alignments between *Z. mays* and *A. thaliana* companion cell development progressions,
974 clustered by k-means into three groups. Distribution of gene-gene distances from the alignments
975 are shown on the right, split by k-mean groups. **h,** Exemplary one-to-one homologs between *A.*
976 *thaliana* and *Z. mays* for the three groups split by pseudotime shifts. Acronyms: CC, companion
977 cell; LRC, lateral root cap; LRP, lateral root primordia. QC, quiescent center; SE, sieve elements.
978
979
980
981
982
983
984
985
986
987
988
989
990
991
992
993
994
995

996 **EXTENDED DATA FIGURE LEGENDS**

997 **Extended Data Fig. 1: Construction of single-cell chromatin accessibility profiles from a**
998 **diverse set of *Zea mays* organs.**

999 **a**, Top; Genome browser screenshot of chromatin accessibility from bulk and single-cell
1000 aggregate ATAC-seq experiments. Chromatin accessibility profiles depict the *tb1* locus and the
1001 *tb1* enhancer located approximately 67-kb upstream. Bottom; binary accessibility scores from a
1002 random selection of 1,000 individual nuclei from each organ. **b,** Spearman's correlation coefficient
1003 matrix comparing bulk and pseudobulk maize ATAC-seq samples across various organs. Sample
1004 codes are shorthand for assay type, sample, and replicate. For example, s-R1 denotes single cell
1005 assay for seminal root replicate 1. The term b-L2 denotes a bulk-ATAC assay for seedling
1006 replicate 2. Codes are as follows: b, bulk; s, single cell; R, seminal root; C, crown root; E, ear; T,
1007 tassel; A, axillary bud; L, seedling. Numbers represent replicate. **c,** Fragment length distributions
1008 across 56,575 cells. The solid line and grey polygon represent the average and standard
1009 deviation, respectively. **d,** Average TSS enrichment (normalized read depth adjusted by the two
1010 windows 1-kb away from TSSs) across all 56,575 nuclei. Grey polygon denotes the standard
1011 deviation. **e**, Genotype-mixing experimental schematic. **f,** Scatterplot of per cell B73 and Mo17
1012 SNP counts from a mixed-genotype experiment (V1 seedlings) colored by genotype classification.
1013 **g,** Posterior probabilities of individual barcodes (rows) highlighting the occurrence of cells with
1014 B73, Mo17, and mixed (doublet) genotype identities. **h,** Genome browser screenshot of traditional
1015 bulk ATAC-seq from 7 day old seedling (row 1), single-cell ATAC-seq from B73 seven day old
1016 seedlings (row 2), pooled B73 and Mo17 nuclei (library ID: Seedling 2) single cell ATAC-seq from
1017 7 day old seedlings (row 3), and the genotype-sorted B73 (row 4) and Mo17 (row 5) alignments
1018 after sorting barcodes by genotype calls from the B73-Mo17 scATAC-seq 7 day old seedling
1019 sample (row 3).

1020

1021 **Extended Data Fig. 2: Cell calling and barcode quality control.**

1022 **a,** Comparison of normalized (0-1) read depths at the union of all peaks across bulk and single-
1023 cell samples (n=265,992) between replicated libraries, and between bulk and single-cell ATAC-
1024 seq assays. **b,** Fragment length distributions for each library. Solid lines indicate the average
1025 distribution across cells within the sample. Grey polygons represent the standard deviation across
1026 nuclei in the library. **c,** Enrichment plots centered on 2-kb windows surrounding TSSs for barcodes
1027 in each tissue. Grey polygons indicate the standard deviation across cells within the noted tissue.
1028 **d,** Density scatter plots of log_{10} transformed barcode read depths (x-axis) by the fraction of Tn5
1029 integration sites mapping to within 2-kb of transcription start sites (TSSs). Dashed red lines
1030 indicate the threshold of two standard deviations from the mean used to filter lower quality
1031 barcodes. **e,** Knee plots illustrating log_{10} transformed cellular read depths of log_{10} ranked barcodes
1032 across libraries. **f,** Density scatter plots of log_{10} transformed barcode read depths (x-axis) by the
1033 fraction of Tn5 integration sites derived from organellar sequences (chloroplast and mitochondrial)
1034 relative to the total number of unique Tn5 integration sites associated with cognate barcode.
1035 Dashed red lines indicate the threshold of two standard deviations from the mean used to filter
1036 lower quality barcodes.
1037

1038 **Extended Data Fig. 3: Clustering metrics and comparison of bulk gene accessibility and**
1039 **expression**

1040 **a**, Parameter regularization of model coefficients (y-axes) with respect to ACR usage (x-axes;
1041 proportion of nuclei with at least one Tn5 integration site in an ACR). **b**, Proportion of variance
1042 captured by the first 26 PCs. Inset: Spearman's correlation of principal components with cell read
1043 depth (log_{10}-transformed). **c**, Number of accessible sites per cell (log_{10}). **d**, Proportion of Tn5
1044 integrations within 2-kb of gene TSSs per cell. **e**, Co-localization of nuclei barcodes from different
1045 biological replicates for three organs. **f**, Comparison of bulk RNA-seq expression levels (y-axis,

1046 log_2 CPM) versus aggregate scATAC-seq gene accessibility scores (x-axis, log_2 CPM) within an
1047 organ.
1048
1049 **Extended Data Fig. 4: Cell-type annotation and GO enrichment**
1050 **a**, UMAP embeddings of nuclei barcodes colored by low (grey) to high (dark purple) gene activity
1051 values of cell-type specific marker genes. **b**, RNA *in situ* hybridization showing expression of
1052 *LOX10* in glume primordia and *GRFTF36* in IM and SMs of staminate inflorescence; *LRR445* in
1053 the IM periphery and SPMs and *MYB89* in the IM and suppressed bract primordia of pistillate
1054 inflorescence; Zm00001d038453 in ground tissue of SAM and leaf primordia sections. Gene
1055 accessibility scores and predicted cell-types are shown on the right. *i*, tassel primordia. *ii,* ear
1056 primordia. *iii*, SAM/leaf. Black triangles point to the glume primordia. Red triangles point to cryptic
1057 bract primordia. Size bars illustrate 100-um. AM, axillary meristem; BS, bundle sheath; GC, guard
1058 cell; GM, ground meristem; GMC, guard mother cell; GP, glume primordia; IM, inflorescence
1059 meristem; L1, layer 1; LFM, lower floral meristem; SAM, shoot apical meristem; SBP, suppressed
1060 bract primordia; SM, spikelet meristem; SPM; spikelet pair meristem; Stomatal PC, stomatal
1061 precursor; UKN, unknown; VEMI, vascular/epidermal meristematic identity; VP, vascular
1062 parenchyma; XP, xylem parenchyma. **c,** Proportion of cells within subcluster (column) derived
1063 from one of six organs (rows). **d,** Distribution of GO term enrichment across clusters, where the
1064 x-axis indicates the number of clusters in which a GO term is significantly enriched.
1065
1066 **Extended Data Fig. 5: Chromatin accessibility variation across plant cell-types**
1067 **a**, Row chromatin accessibility Z-scores across cell-types. Cell-type and subcluster labels are
1068 located adjacent to the heatmap in identical order as the matrix. The first number after the cell-
1069 type label indicates the major cluster number, while the second number represents the subcluster
1070 ID. Legend colors: top left triangle, subcluster (corresponds to the sub-cluster annotation on
1071 heatmap). bottom right triangle, major cluster (corresponds to the major cluster annotation on

1072 heatmap). **b**, Row gene accessibility Z-scores across cell-types. **c**, Proportion of cells derived
1073 from one of six organs within each cell-type/subcluster.
1074
1075 **Extended Data Fig. 6: Transcription factor motif variation underly dynamic accessible**
1076 **regions**
1077 **a**, Comparison of cell-type specific ACR counts (by cell-type) and the number of unique Tn5
1078 integration sites. **b,** Proportion of distal, genic and proximal ACRs per cell-type. **c**, Ranked TF
1079 motif variability across cells, colored by TF family. **d**, Mean TF family motif enrichment (average
1080 deviation scores per cell-type per TF family) across cell-types scaled to +/- 1. **e**, Spearman's
1081 correlation coefficient (rho) between TF motifs (comparison of motif deviations across all nuclei).
1082 Row and column colors represent TF motif families. **f,** TF motif deviations for 440 TF motifs
1083 (columns) per nucleus (rows). The TF family for each corresponding motif is denoted by column
1084 header colors. Cluster identification (sub-cluster/major cluster) are illustrated as row header colors
1085 on the right side of the heatmap. **g**, Relative gene accessibility scores for 2,423 maize
1086 transcription factors (columns) for 50,640 nuclei (rows). Nuclei are sorted by sub-cluster cell-type
1087 (row color labels). A cell-type annotation color legend applicable to panels **b**, **f**, and **g** where left
1088 triangle reflects sub-cluster, right triangle indicates the major cluster.
1089
1090 **Extended Data Fig. 7: Co-accessible ACRs reflect in vivo chromatin interactions and are**
1091 **driven by coordinated TF activity**
1092 **a**, Proportions of co-accessible ACR types, illustrated by toy examples. **b**, Proportion leaf Hi-C,
1093 H3K4me3-HiChIP and H3K27me3-HiChIP chromatin loops that overlap co-accessible ACRs from
1094 leaf cell-types (clusters with greater than 50% of cell derived from seedlings). **c**, Top, $\log_{10}$ number
1095 of connections per ACR per cell-type from all co-accessible ACRs split by genomic context: distal,
1096 proximal, and genic. Bottom, $\log_{10}$ number of connections per ACR per cell-type from cell-type
1097 specific (purple) and constitutive (grey) co-accessible ACRs, split by genomic context. **d,**

1098 Proportion of co-accessible classifications by cell-type for all co-accessible ACRs (top) and cell-
1099 type specific co-accessible ACRs (bottom). **e**, Jaccard similarity of motif composition between co-
1100 accessible ACR edges by cell-type (colored diamonds) relative to the same number of random
1101 ACR-ACR links, permuted 1,000 times for each cell-type (grey boxplots). Box plots represent the
1102 interquartile range, grey lines indicate the permuted range. **f**, Heatmaps of observed proportion
1103 of co-accessible ACRs with the same motif embedded within link edges subtracted and divided
1104 by the expected proportion estimated by 1,000 permutations using random ACR-ACR links with
1105 the same number of co-accessible ACRs. **g,** Exemplary motifs enriched in reciprocal co-
1106 accessible ACRs for *TCP, AP2-EREB,* and *LBD* TF families.

1107

1108 **Extended Data Fig. 8: Pseudotime trajectory construction**

1109 **a,** Overview of pseudotime developmental trajectory analysis from four organs: root, seedling,
1110 tassel (staminate inflorescence), and ear (pistilate inflorescence). **b,** Endodermis development in
1111 crown roots. **c,** Cortex development in crown roots. **d,** Pericycle development in embryonic roots.
1112 **e,** Atrichoblast development in crown roots. **f,** Trichoblast development in crown roots. **g,**
1113 Trichoblast development in embryonic roots. **h,** Lateral root cap (LRC) development in crown
1114 roots. **i,** Lateral root cap (LRC) development in embryonic roots. **j,** Phloem sieve element (SE)
1115 development in crown roots. **k,** Companion cell development in crown roots. **l,** Phloem sieve
1116 element (SE) development in embryonic roots. **m,** Xylem development in crown roots. **n,** Xylem
1117 development in embryonic roots. **o,** Procambial development in crown roots. **p,** Guard cell
1118 development in seedling. **q,** Subsidiary cell development in seedlings. **r,** Floral primordia
1119 development in staminate inflorescence (tassel). **s,** Floral primordia development in pistilate
1120 inflorescence (ear).

1121

1122 **Extended Data Fig. 9: *Arabidopsis thaliana* root cell-type atlas**

1123 **a,** Knee plots for *A. thaliana* root samples illustrating log_{10} transformed cellular read depths of
1124 log_{10} ranked barcodes across two biological replicates. **b,** Density scatter plots of log_{10}
1125 transformed barcode read depths (x-axis) by the fraction of Tn5 integration sites derived from
1126 organellar sequences (chloroplast and mitochondrial) relative to the total number of unique Tn5
1127 integration sites associated with each barcode from the two biological replicates. Dashed red lines
1128 indicate the threshold of two standard deviations from the mean used to filter lower quality
1129 barcodes. **c,** Density scatter plots of log_{10} transformed barcode read depths (x-axis) by the fraction
1130 of Tn5 integration sites mapping to within 2-kb of transcription start sites (TSSs). Dashed red lines
1131 indicate the threshold of two standard deviations from the mean used to filter lower quality
1132 barcodes. **d,** Average TSS enrichment (normalized read depth adjusted by the two 10-bp windows
1133 1-kb away from TSSs) across 5,001 *A. thaliana* root barcodes (rows). **e,** UMAP (Uniform manifold
1134 approximation projection) embeddings of *A. thaliana* root barcodes colored by biological replicate.
1135 **f,** total number of accessible chromatin regions (ACRs). **g,** the proportion of Tn5 integration sites
1136 within 1-kb of TSSs. **h,** Relative gene accessibility for 27 known cell-type/domain restricted marker
1137 genes used to inform cell-type annotation of *A. thaliana* root clusters. **i,** Relative motif deviations
1138 for transcription factors with known cell-type specificities.
1139

1140 **Extended Data Fig. 10: Dynamic and conserved chromatin accessibility across pseudotime**
1141 **between *Arabidopsis thaliana* and *Zea mays***

1142 **a,** Pseudotime trajectories for Atrichoblast, Trichoblast, Lateral root cap (LRC), Cortex,
1143 Endodermis, Lateral root primordia (LRP), Companion cells (CC), and Xylem development. **b,**
1144 Averaged alignments of conserved, shift early *Z. mays*, and shift early *A. thaliana* putative
1145 orthologs. **c,** Pseudotime shifts of TF motifs between *A. thaliana* and *Z. mays*, clustered into k-
1146 means and conserved groups. **d,** Distributions of motif-motif normalized distances between *Z.*
1147 *mays* and *A. thaliana* for the three groups. **e,** Conserved motifs (n=142) ordered by pseudotime.
1148 Heatmaps for *A. thaliana* and *Z. mays* have identical row orders. **f,** Averaged alignments of

1149 conserved, shift early *Z. mays*, and shift early *A. thaliana* groups based on motif-motif global
1150 alignments from the dynamic time-warping algorithm. **g,** Examples of conserved, shift early *Z.*
1151 *mays*, and shift early *A. thaliana* motifs from both species. **h,** Gene expression Z-scores across
1152 *A. thaliana* FAC sorted root cell-types for the TFs recognizing the top four conserved motifs.
1153
1154
1155
1156
1157
1158
1159
1160
1161
1162
1163
1164
1165
1166
1167
1168
1169
1170
1171
1172
1173
1174

1175 **REFERENCES**

1176 1 Cusanovich, D. A. *et al.* A Single-Cell Atlas of In Vivo Mammalian Chromatin Accessibility.
1177 *Cell* **174**, 1309-1324 e1318, doi:10.1016/j.cell.2018.06.052 (2018).

1178 2 Marand, A. P., Zhang, T., Zhu, B. & Jiang, J. Towards genome-wide prediction and
1179 characterization of enhancers in plants. *Biochim Biophys Acta Gene Regul Mech* **1860**,
1180 131-139, doi:10.1016/j.bbagrm.2016.06.006 (2017).

1181 3 Teale, W. D., Paponov, I. A. & Palme, K. Auxin in action: signalling, transport and the
1182 control of plant growth and development. *Nat Rev Mol Cell Biol* **7**, 847-859,
1183 doi:10.1038/nrm2020 (2006).

1184 4 Wittkopp, P. J. & Kalay, G. Cis-regulatory elements: molecular mechanisms and
1185 evolutionary processes underlying divergence. *Nat Rev Genet* **13**, 59-69,
1186 doi:10.1038/nrg3095 (2011).

1187 5 Lu, Z. *et al.* The prevalence, evolution and chromatin signatures of plant regulatory
1188 elements. *Nat Plants* **5**, 1250-1259, doi:10.1038/s41477-019-0548-z (2019).

1189 6 Andersson, R. & Sandelin, A. Determinants of enhancer and promoter activities of
1190 regulatory elements. *Nat Rev Genet* **21**, 71-87, doi:10.1038/s41576-019-0173-8 (2020).

1191 7 Long, H. K., Prescott, S. L. & Wysocka, J. Ever-Changing Landscapes: Transcriptional
1192 Enhancers in Development and Evolution. *Cell* **167**, 1170-1187,
1193 doi:10.1016/j.cell.2016.09.018 (2016).

1194 8 Chang, Y. M. *et al.* Characterizing regulatory and functional differentiation between maize
1195 mesophyll and bundle sheath cells by transcriptomic analysis. *Plant Physiol* **160**, 165-177,
1196 doi:10.1104/pp.112.203810 (2012).

1197 9 Langdale, J. A., Lane, B., Freeling, M. & Nelson, T. Cell lineage analysis of maize bundle
1198 sheath and mesophyll cells. *Dev Biol* **133**, 128-139, doi:10.1016/0012-1606(89)90304-7
1199 (1989).

1200 10 Ricci, W. A. *et al.* Widespread long-range cis-regulatory elements in the maize genome.
1201 *Nat Plants* **5**, 1237-1249, doi:10.1038/s41477-019-0547-0 (2019).

1202 11 Oka, R. *et al.* Genome-wide mapping of transcriptional enhancer candidates using DNA
1203 and chromatin features in maize. *Genome Biol* **18**, 137, doi:10.1186/s13059-017-1273-4
1204 (2017).

1205 12 Crisp, P. A. *et al.* Stable unmethylated DNA demarcates expressed genes and their cis-
1206 regulatory space in plant genomes. *Proc Natl Acad Sci U S A*,
1207 doi:10.1073/pnas.2010250117 (2020).

1208 13 Zhao, H. *et al.* Proliferation of Regulatory DNA Elements Derived from Transposable
1209 Elements in the Maize Genome. *Plant Physiol* **176**, 2789-2803, doi:10.1104/pp.17.01467
1210 (2018).

1211 14 Clark, R. M., Wagler, T. N., Quijada, P. & Doebley, J. A distant upstream enhancer at the
1212 maize domestication gene tb1 has pleiotropic effects on plant and inflorescent
1213 architecture. *Nat Genet* **38**, 594-597, doi:10.1038/ng1784 (2006).

1214 15 Noshay, J. M. *et al.* Cis-regulatory elements within TEs can influence expression of nearby
1215 maize genes. *bioRxiv*, 2020.2005.2020.107169, doi:10.1101/2020.05.20.107169 (2020).

1216 16 Rebeiz, M. & Tsiantis, M. Enhancer evolution and the origins of morphological novelty.
1217 *Curr Opin Genet Dev* **45**, 115-123, doi:10.1016/j.gde.2017.04.006 (2017).

1218 17 Villar, D. *et al.* Enhancer evolution across 20 mammalian species. *Cell* **160**, 554-566,
1219 doi:10.1016/j.cell.2015.01.006 (2015).

1220 18 Wallace, J. G. *et al.* Association mapping across numerous traits reveals patterns of
1221 functional variation in maize. *PLoS Genet* **10**, e1004845,
1222 doi:10.1371/journal.pgen.1004845 (2014).

1223 19 Wang, B. *et al.* Genome-wide selection and genetic improvement during modern maize
1224 breeding. *Nat Genet* **52**, 565-571, doi:10.1038/s41588-020-0616-3 (2020).

1225 20 Gage, J. L., White, M. R., Edwards, J. W., Kaeppler, S. & de Leon, N. Selection Signatures
1226 Underlying Dramatic Male Inflorescence Transformation During Modern Hybrid Maize
1227 Breeding. *Genetics* **210**, 1125-1138, doi:10.1534/genetics.118.301487 (2018).

1228 21 Verweij, W. *et al.* Functionally Similar WRKY Proteins Regulate Vacuolar Acidification in
1229 Petunia and Hair Development in Arabidopsis. *Plant Cell* **28**, 786-803,
1230 doi:10.1105/tpc.15.00608 (2016).

1231 22 Gomez-Mena, C., de Folter, S., Costa, M. M., Angenent, G. C. & Sablowski, R.
1232 Transcriptional program controlled by the floral homeotic gene AGAMOUS during early
1233 organogenesis. *Development* **132**, 429-438, doi:10.1242/dev.01600 (2005).

1234 23 Pliner, H. A. *et al.* Cicero Predicts cis-Regulatory DNA Interactions from Single-Cell
1235 Chromatin Accessibility Data. *Mol Cell* **71**, 858-+, doi:10.1016/j.molcel.2018.06.044
1236 (2018).

1237 24 Gate, R. E. *et al.* Genetic determinants of co-accessible chromatin regions in activated T
1238 cells across humans. *Nat Genet* **50**, 1140-1150, doi:10.1038/s41588-018-0156-2 (2018).

1239 25 Satpathy, A. T. *et al.* Massively parallel single-cell chromatin landscapes of human
1240 immune cell development and intratumoral T cell exhaustion. *Nat Biotechnol* **37**, 925-936,
1241 doi:10.1038/s41587-019-0206-z (2019).

1242 26 Buenrostro, J. D. *et al.* Single-cell chromatin accessibility reveals principles of regulatory
1243 variation. *Nature* **523**, 486-490, doi:10.1038/nature14590 (2015).

1244 27 Peng, Y. *et al.* Chromatin interaction maps reveal genetic regulation for quantitative traits
1245 in maize. *Nat Commun* **10**, 2632, doi:10.1038/s41467-019-10602-5 (2019).

1246 28 Sun, Y. *et al.* 3D genome architecture coordinates trans and cis regulation of differentially
1247 expressed ear and tassel genes in maize. *Genome Biol* **21**, 143, doi:10.1186/s13059-020-
1248 02063-7 (2020).

1249 29 Chuck, G. S., Brown, P. J., Meeley, R. & Hake, S. Maize SBP-box transcription factors
1250 unbranched2 and unbranched3 affect yield traits by regulating the rate of lateral primordia
1251 initiation. *Proc Natl Acad Sci U S A* **111**, 18775-18780, doi:10.1073/pnas.1407401112
1252 (2014).

1253 30 Heger, P., Marin, B., Bartkuhn, M., Schierenberg, E. & Wiehe, T. The chromatin insulator
1254 CTCF and the emergence of metazoan diversity. *Proc Natl Acad Sci U S A* **109**, 17507-
1255 17512, doi:10.1073/pnas.1111941109 (2012).

1256 31 Liu, C., Cheng, Y. J., Wang, J. W. & Weigel, D. Prominent topologically associated
1257 domains differentiate global chromatin packing in rice from Arabidopsis. *Nat Plants* **3**, 742-
1258 748, doi:10.1038/s41477-017-0005-9 (2017).

1259 32 Karaaslan, E. S. *et al.* Marchantia TCP transcription factor activity correlates with three-
1260 dimensional chromatin structure. *Nat Plants*, doi:10.1038/s41477-020-00766-0 (2020).

1261 33 Takacs, E. M. *et al.* Ontogeny of the maize shoot apical meristem. *Plant Cell* **24**, 3219-
1262 3234, doi:10.1105/tpc.112.099614 (2012).

1263 34 Somssich, M., Je, B. I., Simon, R. & Jackson, D. CLAVATA-WUSCHEL signaling in the
1264 shoot meristem. *Development* **143**, 3238-3248, doi:10.1242/dev.133645 (2016).

1265 35 Jiang, K., Zhu, T., Diao, Z., Huang, H. & Feldman, L. J. The maize root stem cell niche: a
1266 partnership between two sister cell populations. *Planta* **231**, 411-424,
1267 doi:10.1007/s00425-009-1059-3 (2010).

1268 36 Wallner, E. S. *et al.* Strigolactone- and Karrikin-Independent SMXL Proteins Are Central
1269 Regulators of Phloem Formation. *Curr Biol* **27**, 1241-1247, doi:10.1016/j.cub.2017.03.014
1270 (2017).

1271 37 Baker, R. F. *et al.* Sucrose Transporter ZmSut1 Expression and Localization Uncover New
1272 Insights into Sucrose Phloem Loading. *Plant Physiol* **172**, 1876-1898,
1273 doi:10.1104/pp.16.00884 (2016).

1274 38 Kajala, K. *et al.* Innovation, conservation and repurposing of gene function in plant root
1275 cell type development. *bioRxiv*, 2020.2004.2009.017285, doi:10.1101/2020.04.09.017285
1276 (2020).

1277 39 Brady, S. M. *et al.* A high-resolution root spatiotemporal map reveals dominant expression
1278 patterns. *Science* **318**, 801-806, doi:10.1126/science.1146265 (2007).

1279 40 You, Y. *et al.* Phloem Companion Cell-Specific Transcriptomic and Epigenomic Analyses
1280 Identify MRF1, a Regulator of Flowering. *Plant Cell* **31**, 325-345,
1281 doi:10.1105/tpc.17.00714 (2019).

41 Jiang, H., Li, H., Bu, Q. & Li, C. The RHA2a-interacting proteins ANAC019 and ANAC055 may play a dual role in regulating ABA response and jasmonate response. *Plant Signaling & Behavior* **4**, 464-466, doi:10.4161/psb.4.5.8543 (2009).

42 Yamaguchi, M. *et al.* VND-INTERACTING2, a NAC domain transcription factor, negatively regulates xylem vessel formation in Arabidopsis. *Plant Cell* **22**, 1249-1263, doi:10.1105/tpc.108.064048 (2010).

43 Jiao, Y. *et al.* Improved maize reference genome with single-molecule technologies. *Nature* **546**, 524-527, doi:10.1038/nature22971 (2017).

44 Li, H. *et al.* The Sequence Alignment/Map format and SAMtools. *Bioinformatics* **25**, 2078-2079, doi:10.1093/bioinformatics/btp352 (2009).

45 AFA Smit, R. H., and P Green. *RepeatMasker Open-4.0* (2013-2015).

46 Camacho, C. *et al.* BLAST+: architecture and applications. *BMC Bioinformatics* **10**, 421, doi:10.1186/1471-2105-10-421 (2009).

47 Team, R. C. *R: A language and environment for statistical computing.*, <http://www.R-project.org/> (2013).

48 Chen, S., Zhou, Y., Chen, Y. & Gu, J. fastp: an ultra-fast all-in-one FASTQ preprocessor. *Bioinformatics* **34**, i884-i890, doi:10.1093/bioinformatics/bty560 (2018).

49 Li, H. Aligning sequence reads, clone sequences and assembly contigs with BWA-MEM. *arXiv e-prints*, arXiv:1303.3997 (2013). <https://ui.adsabs.harvard.edu/abs/2013arXiv1303.3997L>.

50 Garrison, E. & Marth, G. Haplotype-based variant detection from short-read sequencing. *arXiv e-prints*, arXiv:1207.3907 (2012). <https://ui.adsabs.harvard.edu/abs/2012arXiv1207.3907G>.

51 Zhang, Y. *et al.* Model-based analysis of ChIP-Seq (MACS). *Genome Biol* **9**, R137, doi:10.1186/gb-2008-9-9-r137 (2008).

52 Hafemeister, C. & Satija, R. Normalization and variance stabilization of single-cell RNA-seq data using regularized negative binomial regression. *Genome Biol* **20**, doi:ARTN 296 10.1186/s13059-019-1874-1 (2019).

53 Witten, D. M., Tibshirani, R. & Hastie, T. A penalized matrix decomposition, with applications to sparse principal components and canonical correlation analysis. *Biostatistics* **10**, 515-534, doi:10.1093/biostatistics/kxp008 (2009).

54 Stuart, T. *et al.* Comprehensive Integration of Single-Cell Data. *Cell* **177**, 1888-+, doi:10.1016/j.cell.2019.05.031 (2019).

55 Corces, M. R. *et al.* The chromatin accessibility landscape of primary human cancers. *Science* **362**, doi:10.1126/science.aav1898 (2018).

1317 56 Fang, R. *et al.* SnapATAC: A Comprehensive Analysis Package for Single Cell ATAC-
1318 seq. *bioRxiv*, 615179, doi:10.1101/615179 (2020).

1319 57 Robinson, M. D., McCarthy, D. J. & Smyth, G. K. edgeR: a Bioconductor package for
1320 differential expression analysis of digital gene expression data. *Bioinformatics* **26**, 139-
1321 140, doi:10.1093/bioinformatics/btp616 (2010).

1322 58 Grant, C. E., Bailey, T. L. & Noble, W. S. FIMO: scanning for occurrences of a given motif.
1323 *Bioinformatics* **27**, 1017-1018, doi:10.1093/bioinformatics/btr064 (2011).

1324 59 O'Malley, R. C. *et al.* Cistrome and Epicistrome Features Shape the Regulatory DNA
1325 Landscape. *Cell* **166**, 1598, doi:10.1016/j.cell.2016.08.063 (2016).

1326 60 Galli, M. *et al.* The DNA binding landscape of the maize AUXIN RESPONSE FACTOR
1327 family. *Nat Commun* **9**, 4526, doi:10.1038/s41467-018-06977-6 (2018).

1328 61 Schep, A. N., Wu, B., Buenrostro, J. D. & Greenleaf, W. J. chromVAR: inferring
1329 transcription-factor-associated accessibility from single-cell epigenomic data. *Nat*
1330 *Methods* **14**, 975-978, doi:10.1038/nmeth.4401 (2017).

1331 62 Granja, J. M. *et al.* ArchR: An integrative and scalable software package for single-cell
1332 chromatin accessibility analysis. *bioRxiv*, 2020.2004.2028.066498,
1333 doi:10.1101/2020.04.28.066498 (2020).

1334 63 Emms, D. M. & Kelly, S. OrthoFinder: phylogenetic orthology inference for comparative
1335 genomics. *Genome Biol* **20**, 238, doi:10.1186/s13059-019-1832-y (2019).

1336 64 van Dijk, D. *et al.* Recovering Gene Interactions from Single-Cell Data Using Data
1337 Diffusion. *Cell* **174**, 716-729 e727, doi:10.1016/j.cell.2018.05.061 (2018).

1338 65 Alpert, A., Moore, L. S., Dubovik, T. & Shen-Orr, S. S. Alignment of single-cell trajectories
1339 to compare cellular expression dynamics. *Nat Methods* **15**, 267-270,
1340 doi:10.1038/nmeth.4628 (2018).

1341 66 Hofmeister, B. T. & Schmitz, R. J. Enhanced JBrowse plugins for epigenomics data
1342 visualization. *BMC Bioinformatics* **19**, 159, doi:10.1186/s12859-018-2160-z (2018).
1343